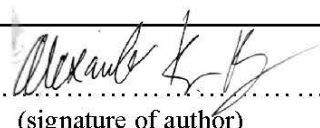




Universitetet
i Stavanger

FACULTY OF SCIENCE AND TECHNOLOGY

MASTER'S THESIS

Study programme/specialisation: Master of Science in Engineering Structures and Materials	Spring semester, 2018 Open
Author: Alexander Kalvik Berg	 (signature of author)
Programme coordinator: Vidar Hansen Supervisor(s): Mette Nedreberg	
Title of master's thesis: "EBSD and TEM study of DMD manufactured cp-Ti (grade 2)"	
Credits:	
Keywords: EBSD TEM Comercially pure titanium (grade 2) Direct metal deposition	Number of pages: 54 +supplemental material/other: 3 Stavanger, 29.06.2018 date/year

Abstract

Two components, 3D printed by Norsk Titanium components, through a direct metal deposition plasma transferred arc. An additive layer manufacturing technique. One made of a single wire layer thin sample, and one made of two wires thick sample. These components were to be studied through transmission electron microscope (TEM) and through the use of electron backscattering diffraction (EBSD) detector. Electrochemical polishing was used for etchant, to avoid using hydrofluoric acid because of its volatile nature. During the thesis it was also a point to see what kind of deformations the electrochemical polishing would uncover. During the TEM study it was found that the components a dislocation density in the order of 10^9cm^{-2} . The flow stress was calculated to be average 298MPa because of the dislocation density. The ratio of the different dislocation types was measured and calculated in TEM through a technique called weak beam together with $\mathbf{g} \cdot \mathbf{b}=0$ criterion. The density of pure edge was found to be $1,84 * 10^9 \text{cm}^{-2}$ in an area which contained $3,19 * 10^9 \text{cm}^{-2}$. Leading to a higher density of pure edge dislocation compared to mix and screw dislocation. Strain energy for edge dislocation is about 50% higher than screw, which leads to higher strain energy for the area. The stress field for edge dislocation is increased by the same amount. Through the TEM in a complete α -phase areas, elongated β structures were found. Through the use of the EBSD, the two wire component with a non-machined inside were studied. Small fraction of β -phase on the inside of the component was discovered. This is the area exposed to the argon atmosphere during manufacturing. For β -phase to be retained, the cooling rate must have been sufficiently high. Above a critical point of $15^\circ\text{C}/\text{s}$. The middle and outside of the component had no detectable β -phase. Meaning that the cooling rate is higher where it was exposed to argon gas. This could mean that heat dissipation is not high enough in the metal to form retained β -phase and the heat dissipates more quickly to gaseous environment. Tensile twinning were discovered matching $\{10\bar{1}2\}\langle\bar{1}011\rangle$. These twinning deformations were observed through the sample. In the two wire made component, increased twinning were observed in the middle of the horizontal plane (XY) and could be the area of the two wires overlapping. The misdirection angles showed peaks of 60° and 90° corresponding to the misorientation planes of the phase transformation of $\langle 110 \rangle \beta$ to hcp which is either 60° or 90° . Comparing the vertical and the horizontal plane of the thin sample made of one wire. Elongated grains were seen in the vertical plane corresponding to columnar grains in the epitaxial growth direction. The misorientation angles peaked at 60° corresponding to the $\langle 110 \rangle \beta$ plane transformation which favors the 60° .

Acknowledgements

Sincerest thanks goes to the following person who have been a tremendous help with the thesis. They have gone above and beyond what would normally be considered. They have provided me with the help, the information and ideas. Challenged me, and encouraged me in every step of the way. This thesis could not have done with without them

Professor Vidar Folke Hansen (UIS)

I would like to thank my course supervisor, for his education and advice. His help and guidance in order to overcome the challenges have been a tremendous help.

Wakshum Mekonnen Tucho, Senior engineer at UIS

His help and knowledge with the electron microscopes, and with the help with preparing the samples have been paramount to this thesis. His help with the electronbackscatter diffraction detector have been an enlightening experience.

Andreas Delimitis, Post-doctor at UIS

His vast knowledge of material science have helped put the information in place, and was a great resource. He helped to enlighten and challenge with the tougher subjects on material science. His help with the TEM helped carry this thesis, and pushed it. His explanations of the science helped me gain a better understanding of the subjects. He went beyond any expectations with always being ready to help.

And I would like to thank Roll Royce marine for giving me the opportunity to write this thesis. And for Norsk Titanium Components AS for making the samples used in the thesis.

List of abbreviations

DMD	Direct Metal Deposition
ALM	Additive Layer Manufacturing
SEM	Scanning Electron Microscope
TEM	Transmission electron microscope
HAZ	Heat affected zone
SE	Secondary electrons
EBSD	Electron BackScatter Diffraction
HCP	Hexagonal Close Packed
BCC	Body Centered Cube
IPF	Inverse Pole Figure
NTiC	Norsk Titanium Components
CAD	Computer Aided Design
CP-Ti	Commercially pure Titanium (in this case, grade 2 titanium)
VLM	Visual Light Microscopy
BF	Bright Field
DF	Dark Field
WB	Weak Beam
<i>g</i>	Reciprocal lattice vector
<i>b</i>	Burgers vector

Table of Contents

Abstract.....	iii
Acknowledgements.....	vi
List of abbreviations.....	vii
1 Introduction	1
1.1 Objective	3
2 Theoretical foundation and background	4
2.1 Titanium and titanium alloys	4
2.1.1 Crystal structure of titanium.....	6
2.2 Direct metal deposition	7
2.3 Phase transformation	8
2.3.1 Solidification.....	9
2.3.2 Solid allotropic transformation from β to α and HAZ	10
2.4 Deformation Modes.....	12
2.4.1 Slip modes and dislocations.....	12
2.4.2 Dislocations	13
2.4.3 Dislocation Density and its relationship to stress	15
2.4.4 Deformation twinning.....	15
2.5 EBSD	17
2.5.1 Inverse pole figure	18
2.6 TEM	19
3 Experimentation	21
3.1 Preparation	22
3.1.1 Cutting.....	23
3.1.2 Grinding and polishing	24
3.1.3 Electrochemical polishing	25
3.2 EBSD	25
3.3 EDS experimentation	26
3.4 TEM	26
4 Results.....	30
4.1 EDS	30
4.2 Visual light microscope	32
4.3 TEM	34

4.4	EBSD of thick sample in XY plane.....	43
4.5	EBSD of thin sample in both XY and YZ plane	48
5	Discussion and conclusion	51
6	References	53
	Appendix A.....	i
	Appendix B	ii
	Appendix C	iii

Figure 1-1 Thin sample (left) and thick sample (right). The thin sample is made by using one wire for each layer. The thick sample used two wires.....	3
Figure 2-1 - Binary phase diagram Ti-O (ASM International, u.d.).....	6
Figure 2-2 Crystal structure of hcp α (left) and bcc β (right) (Leyens & Peters., u.d., p. 4).....	7
Figure 2-3 NTiC patent-Creating the wire from titanium particles and heating it with plasma (Norsk Titanium, 2010).....	7
Figure 2-4 Solidification grain direction of welds (Grong, 1997, p. 236).....	9
Figure 2-5 Observations of solidifications from liquid metal to β -phase (Yu-ichi, et al., 2009).....	9
Figure 2-6 β - α transformation according to burgers relationship (Leyens & Peters., u.d., p. 7).....	10
Figure 2-7 β - α transformation in pure titanium (Yu-ichi, et al., 2009).....	10
Figure 2-8 Dynamic CCT diagram for CP-Ti (Chun & Wen-feng, 2010).....	11
Figure 2-9 Optical micrographs of alloys at different cooling rates: (a) 0.5 °C/s; (b) 1 °C/s; (c) 2 °C/s; (d) 5 °C/s; (e) 7 °C/s; (f) 10 °C/s; (g) (Chun & Wen-feng, 2010).....	11
Figure 2-10 Slip planes and slip direction in hcp Ti (Lutjering & Williams, 2007, p. 20).....	12
Figure 2-11 Edge dislocation occurs when slip vector is perpendicular to the AD slip line. (Dieter, 1986).....	13
Figure 2-12 Screw dislocation with the slip vector going parallel to the dislocation line.....	13
Figure 2-13 Schematic drawing showing the process of climbing for edge dislocation (Meyers & Chawla, 2009, p. 270).....	14
Figure 2-14 Schematic view of the tension and compression twinning. Their angles according to the boundary misorientation is shown. (PADILLA, et al., 2007).....	16
Figure 2-15 Schematic drawing of the SEM sample holder at tilt and EBSD detector (Zhou & Wang, 2006, p. 47).....	17
Figure 2-16 An example of an inverse pole figure (Vera, et al., 2017).....	18
Figure 2-17 The various electron incidents reacting from central beam (Williams & Carter, 2009).....	19
Figure 2-18 A cross section view of a column in TEM (Shindo & Oikawa, 2002, p. 15).....	20
Figure 3-1 Top view of the sample is set to plane XY and the initial cut direction is in X direction.....	21
Figure 3-2 Side view of the specimen it set to be the plane YZ.....	21
Figure 3-3 - Finished product made from DMD given by Norsk Titanium (right) and the cut line (right) from top of cone.....	22
Figure 3-4 – Cross section view of the sample. The red lines corresponds to the cuts that were made during preparation. Similar cuts were taken in both the thin and thick sample, which were made by single and dual wire respectively.....	23
Figure 3-5 Thin sample mounted on plexiglass with the use of double sided tape for easier handling in grinding and polishing.....	24
Figure 3-6 Finished cut samples of both the thick and thin.....	24
Figure 3-7 Choosing a diffraction beam with the objective aperture creates a dark field image.....	26
Figure 3-8 Forming two beam condition with center beam and a reflection, g.....	26
Figure 3-9 Diffraction image with a two beam condition formed. With the reflection g forming two beam. Moving the opposite, the -g, into the objective aperture forms a weak beam image.	27
Figure 3-10 Visualization of the [1213] plane.....	28
Figure 3-11 Zone axis of [1213] that matches the d-spacing, ratios and angles to the one in Figure 3-12 (Edington, 1975, pp. 102-103).....	28

Figure 3-12 Indexing done by using Crystbox. The d-space is measured and given. In order to successfully index the d-spaces, angles and ratios must be analyzed and compared to known zone axis' like the one in Figure 3-11. Which matches this one. 28

Figure 4-1 EDS spectra pure titanium 30

Figure 4-2 EDS containing elevated levels of Al, Cl and O 31

Figure 4-3 Comparison of the sample to the study of cooling rates (Chun & Wen-feng, 2010). The etchants used here are different, but comparing the different microstructures made this picture the best comparison. The picture to the right is the picture with 15°C/s. What to look for here is the sharp edges in the grains, and the lines in the grain themselves. This might lead to the possibility that the sample contains retained β -phase because of cooling rate..... 32

Figure 4-4 VLM picture from the sample. A general idea of the microstructure is needed to compare the pictures to study from the cooling rate. The etchants are different so edges might look different..... 32

Figure 4-5 Diffraction image with its corresponding BF image. Zone axis here is [1213]. The reflection chosen for WB imaging is marked with red $\langle 0111 \rangle$ 34

Figure 4-6 Same WB image as Figure 4-6 with the dislocations marked. The dislocations seem to follow a specific line which might mean that this is a slip plane..... 35

Figure 4-7 [1213] $\langle 0111 \rangle$ WB image taken from the area shown in Figure 4-5. The white lines shown here are dislocations. The area here are $15792nm^2$ 35

Figure 4-8 BF image of an area with dislocations. Zone axis of [5143]. The arrows shows the directions. The dislocations seems to generally one of the two. 36

Figure 4-9 Same area as Figure 4-8, with marked dislocations. There are 53 dislocations. The area here is $17832nm^2$ 36

Figure 4-10 Diffraction image from zone axis [0111] with reflections $\langle 1011 \rangle$ (green circle) and $\langle 2110 \rangle$ (red circle) marked. These two reflections are the basis for the weak beam image taken in 37

Figure 4-11 Same Weak beam image from Figure 4-12 with marked dislocations. 45 dislocations are present here..... 38

Figure 4-12 Weak beam image taken from the reflection $\langle 1011 \rangle$ from the diffraction image seen in Figure 4-10. Area is calculated to be $1,40954 * 10 - 8cm^2$ 38

Figure 4-13 Weak beam image taken from $\langle 2110 \rangle$. The criterion $g \cdot b = 0$ is fulfilled for edge dislocations here. The remaining dislocation are marked. The 19 remaining dislocations can only be screw or mixed type. 39

Figure 4-14 Deformed twinning structure with retained β phase..... 41

Figure 4-15 Weak beam image of the reflection in the red circle showing that the outside of the elongated structure belongs to hcp with zone axis [5143] 42

Figure 4-16 Weak beam image formed from the reflection shown in green circle Figure 4-16. This shows that the inside of this this elongated structure is from the system that is from the reflection chosen of $\langle 111 \rangle$ 42

Figure 4-17 Diffraction image with majority of spots corresponding to the hcp crystal with zone axis of [5143]. The reflections that are marked, belong to bcc b_{111} 42

Figure 4-18 Taken from the sample closest to the inside. Where surface is non-machined. The phases are marked with α -phase (red) and β -phase (green). Of the sample taken. This was the only sample with any measurable amount of β -phase. The EBSD showed that it is 98.5% α , and only 0.6% β -phase 43

Figure 4-19 The misorientation angles of the three samples. There are clear peaks located around 60° and 90°. According to (Xu, et al., 2017) these are compression twin (CT) and tension twin (TW). These are marked..... 44

Figure 4-20 The sample taken from the middle of the area (left) shows no β phase. Neither does the sample close to the outside, where the machined surface lies. The phases is marked by red, α-phase. B-phase is marked green, but none is present..... 44

Figure 4-21 Sample taken from the inside sample. The misrotation angle that matches the peaks is shown. Both tensile twin area marked green and compressive twin area marked blue. To the right, a zoomed in view of the twins can be seen along with the crystal orientation. The needle like structures are tensile twins marked with green borders. The compressive twins should have been seen here in blue border. A zoomed in picture of a grain (blue border) with misrotation matching the compression twin can be seen to the right. A small twin can be seen to left in image with green box and green arrow. 45

Figure 4-22 Sample taken from the sample closest to the outside surface. The misorientation peaks seen in Figure 4-19 is marked and color coded. There are no twinning structure. The area that matched the 35° {1121}<1126> twin, does also not show any twinning deformities. 46

Figure 4-23 Sample taken of the middle area. Tensile twins are marked with red arrows {1012}<1011>. The misrotation angle boundaries that matches the compression twin of {1012}<1011> is marked in green. But there is no obvious compression twin structure. 46

Figure 4-24 The inside sample (left), the middle, and outside sample (right). Comparing the samples there is an increasing in the subgrains. The inside has large grains, while the outside sample has smaller subgrains down to ~50μm 47

Figure 4-25 Sample XY from XY plane. Twinning deformity marked in yellow..... 48

Figure 4-26 Sample YZ from YZ plane. The marked boundaries are the most prominent ones..... 48

Figure 4-27 Misorientation angle chart of XY and YZ plane 48

Figure 4-28 A sample from the YZ plane. A grain almost take up the whole sample size..... 49

Figure 4-29 The sample from the XY. Small subgrains here varying from 10-80 micrometer. Although no elongation. The grains have comparable size to the YZ plane, but there are more subgrains here..... 49

Figure 4-30 The sample from the ZY plane with grains marked. The elongated columnar grains are really visible here. 13 49

Figure 4-31 The Sample from XY plane (right) and the YZ plane (left) show that many of the subgrains were once a part of the same grain..... 50

Table 2-1 Commonly used metals and alloys. A comparison of the characteristics. (Lutjering & Williams, 2007, p. 15)	4
Table 2-2 Comparison of Commercially pure titanium and Ti6Al4V (Lutjering & Williams, 2007, p. 34 and 176)	5
Table 2-3 Deformation slip mode of hexagonal titanium	12
Table 2-4 Collected from (Abbaschian & Reed-Hill, 2011) and (P.Rodriguez-Calvillo & J.M.Cabrera, 2015)	15
Table 2-5 Deformation twinning modes for hexagonal titanium (Nervo, et al., 2015)	16
Table 3-1 Grinding steps for EBSD and TEM samples	24
Table 4-1 Density of dislocations from the area shown in Figure 4-5, Figure 4-7 and Figure 4-7	34
Table 4-2 Flow stress calculations, dislocation densities are in m	40

1 Introduction

1 Introduction

The latest on the market for the commonly used structural metals are Titanium and Titanium alloys. Due to the cost, Titanium was formerly regarded as an exotic material and primarily used for purposes which was not cost sensitive. Lately this has seen a change due to mainly two reasons. One is that manufacturing and tooling cost has gone down while there have in some industries been an increased awareness of cost related to reliability and maintenance. This is mainly due to the fact that, while titanium is lighter than steel, it is also stronger than aluminum. It has an intermediate density to steel and aluminum. The melting temperature of titanium is also higher than steel and nickel alloys which is an incentive were creep is an issue. Accounting for density correction biases, titanium even has a higher strength than steel. Titanium is also a very corrosive resistant material. This means that titanium can be used in environments where steel or nickel alloys are not a viable option.

Generally, there are two markets for titanium. One driven by the structural properties, its strength to density ratio. And one driven by its corrosive resistance, and environmental compatibility. The first market is mainly the aerospace industry. Seeing as titanium is light and strong, it's a perfect fit for planes. Titanium was quickly incorporated into jet engines after it was first used. Because of the strength and the ability to handle temperatures up to 550°C. The second market is mainly subsea, marine, and industrial equipment. In recent years, titanium even serves as a biomedical equipment material. Replacing stainless steel and Co-based metals. This is due to titanium's low Young's modulus, shape memory response and high fatigue strength (Banerjee & Williams, n.d.).

The biggest barrier for the use of titanium is the price. From 1950's to 2000 the biggest consumer of titanium was the aerospace industry. After 2000 the industrial use for titanium has surpassed that of aerospace. The reason for the high price is the difficulty of handling titanium. A rule of thumb in the titanium business has been that the price for machining away 1kg, costs as much as producing 1kg of titanium. With increased availability and lower prices, Titanium will proliferate into areas were currently carbon steel or aluminum solutions are dominating, but were Titanium will be a more cost effective concept in a life cycle view. Ironically the largest barrier to the price of titanium, is the price of the material itself.

In an effort to lower the cost of titanium, new methods for production are being developed. To minimize the use of titanium as possible, a method called additive layer manufacturing is used. This means that a

1 Introduction

component is created incrementally by adding materials, layer by layer. Additive layer manufacturing uses less material since it can be built closer to the design specification of the component.

Norsk Titanium patented an additive layer manufacturing method in 2011 (Stempfer, 2011). With the use of direct metal deposition by using a weld wire fed transferred plasma arc, layer on top of layer is applied to reach specified shape. This is one of the more cost-effective additive manufacturing methods. The direct metal deposition transferred plasma arc (DMD-TPA) has a higher (2-3kg per hour) deposition rate than other techniques. In comparison electron beam melting (EB) or laser melting has a deposition rate of about 100-200grams per hour. The DMD-TPA uses a weld wire, whereas most other techniques like EB or laser melting uses spherical powder. The cost of spherical powder is three times the cost of wire. The capital cost of DMD-TPA is in the range of \$700k-\$1M. Comparing to EB and laser melting the price is around \$500k. A 3D printer is in the range of \$20k-\$30k. The when you take in to account the production efficiency, as in price and speed, the DMD-TPA becomes the cheapest. It has a much larger capacity, increased speed, and lowered cost of material.

1 Introduction

1.1 Objective

Rolls Royce marine has 3D-printed two components of Azipull Carbon propeller in titanium. The component is printed with Titanium grade 2, which is referred to as commercially pure titanium. The 3D-printer which the component is manufactured with is an additive layer manufacturing technique. Or more specifically a subsection of additive layer manufacturing calling direct metal deposition plasma transferred arc. One component is made from single wire when layering, and the other uses two wires. The two sample that has been given, can be seen in Figure 1-1. During this thesis the single wire component will be referenced as the thin sample, and the two wire component will be referenced as the thick sample. The thick sample also has a non-machined inside, and this inside surface has been exposed to the argon during manufacturing. The goal of this thesis is to study the microstructure of a finished product that was manufactured in with the DMD-TPA. Instead of using hydrofluoric acid as the basis of the etchant, electrochemical polishing will be used instead. This is because of the volatile nature of HF. Deformation will be studied in the EBSD and TEM. The EBSD will be used to study grain boundaries and deformities that can be seen on μm scale. TEM will be used to study deformities on the nm scale. The dislocation densities will be measured. The ratio of edge to screw dislocation will also be attempted to ascertain



Figure 1-1 Thin sample (left) and thick sample (right). The thin sample is made by using one wire for each layer. The thick sample used two wires.

2 Theoretical foundation and background

2 Theoretical foundation and background

In this part of the thesis the foundation of theoretical knowledge is given. Titanium and its alloys will be covered, as well as background on additive manufacturing. The foundational knowledge on Norsk titanium's direct metal deposit wire weld transferred plasma arc will also be given.

2.1 Titanium and titanium alloys

Table 2-1 Commonly used metals and alloys. A comparison of the characteristics. (Lutjering & Williams, 2007, p. 15)

	Ti	Fe	Ni	Al
Melting Temperature (°C)	1670	1538	1455	660
Allotropic Transformation (°C)	882	912		
Crystal Structure	β $\xrightarrow{882}$ α	γ $\xrightarrow{912}$ α	fcc	fcc
Room Temperature E (GPa)	115	215	200	72
Yield Stress Level (MPa)	1000 α	1000#	1000*	500 \S
Density (g/cm ³)	4.5	7.9	8.9	2.7
Comparative Corrosion Resistance	Very High	Low	Medium	High
Comparative Reactivity with Oxygen	Very High	Low	Low	High
Comparative Price of Metal	Very High	Low	High	Medium

α Ti6Al4V, #high strength steel, *Superalloy, \S heat-treatable Al alloy

Titanium (Ti) is a transition element belonging to group 4 of the periodic table (1). It has a molecular atomic weight of 47.867 g/mol. There are two crystal structure for when pure titanium is in solid state. The two allotropes, α -phase and β -phase is each only stable at different temperatures. The β -transus temperature of pure titanium is at $882\pm 2^\circ\text{C}$. Below this temperature is the domain of α -titanium, and above is the β -titanium. In there is a comparison of commonly used metals, and pure titanium shows the best strength compared to density, the highest melting point and even the best corrosion resistance. Some titanium alloys can even reach as high as 1000MPa in yield strength. The light weight competitor of titanium is aluminum. But titanium has an advantage where temperature reaches above 150°C . The high reactivity of titanium towards oxygen leads to stable and adherent oxide layer when exposed oxygen. This results in the high corrosion resistance of the titanium. The high reactivity of the oxygen also limits the use of titanium. If used in applications where temperature reaches above 600°C , the diffusion of oxygen through the oxide layer increase and causes embrittlement (Lutjering & Williams, 2007, pp. 1-4) (Lutjering & Williams, 2007, p. 15).

2 Theoretical foundation and background

Table 2-2 Comparison of Commercially pure titanium and Ti6Al4V (Lutjering & Williams, 2007, p. 34 and 176)

Grade or Alloy	O (max.)	Fe (max.)	σ 0.2(MPa)	T β (°C)
CP Titanium				
CP Titanium Grade 1	0.18	0.20	170	890
CP Titanium Grade 2	0.25	0.30	275	915
CP Titanium Grade 3	0.35	0.30	380	920
CP Titanium Grade 4	0.40	0.50	480	950
Ti-6Al-4V Grade 5	0.20	0.25		995

The types of titanium alloying materials are categorized as to how it alters the β -transus line. The classifications are neutral, α -stabilizing and β -stabilizing. β -stabilizers like, V, Mo, Nb, Hf, Ta, Mn, Cr, Cu, Ni, Fe, Co, Au, Ag, W and H lowers the β -transus line. This allows for β -phase to form at lower temperature. The α -stabilizers, Al, Ga, B, Sc, La, Ce, C, O and N, allow the α -phase to form at higher temperatures. Neutral elements change the β -transus line very little, to no effect. The grade 2 titanium is what is known as commercially pure titanium, which means it has a high % of titanium, 98%. It is the most commonly used of the commercially pure titanium. The tensile strength levels are between 390 and 540Mpa. (Leyens & Peters., u.d., pp. 9-19). In the tests at Norsk titanium, the ultimate tensile strength of the grade 2 was 419Mpa on the axis parallel to the build layer, and 409Mpa on the perpendicular axis (Norsk Titanium, 2010). The most commonly out of all the titanium's grades is the grade 5, Ti-6Al-4V. It is known as a $\alpha+\beta$ alloy. It has a good balance of properties. Al is a α -stabilizer, and V is β -stabilizer. It is the most intensively developed and tested titanium alloy and is a good reference point to compare. (Leyens & Peters., u.d., pp. 19-22). In Table 2-2 there is a comparison of the various commercially pure titanium, the grade 5 alloy and their chemical composition. The difference in grade 1-4 is the oxygen content. The Fe is treated as an impurity. In Figure 2-1 the phase diagram for Ti-O is shown. Seeing as oxygen is a α -stabilizer it will shift the β -transus to a higher position. The transus line is noted in Table 2-2.

2 Theoretical foundation and background

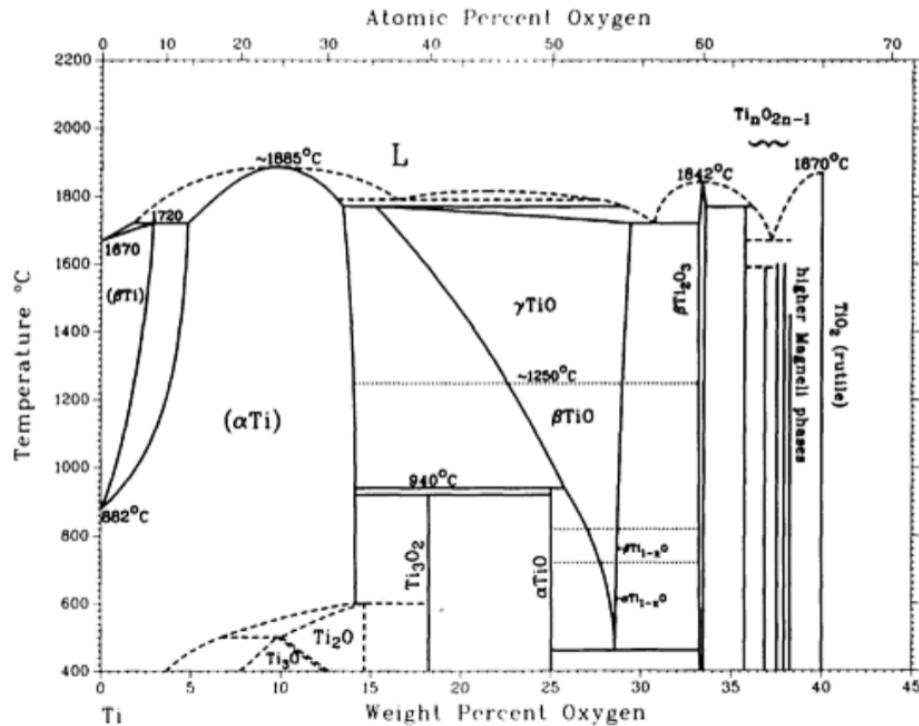


Figure 2-1 - Binary phase diagram Ti-O (ASM International, u.d.)

2.1.1 Crystal structure of titanium

As mentioned previously, pure titanium exhibits an allotropic phase transformation at $882 \pm 2^\circ\text{C}$. When going above this temperature, pure titanium changes from hexagonal close packed crystal, α -phase. To the body-centered cubic crystal structure, β -phase. The temperature of the transformation may vary depending on the purity of the titanium. The transformation temperature is strongly influenced by interstitial and substitutional elements. The hexagonal close packed crystal structure (hcp) in the α -phase is shown in Figure 2-2. The crystal structure of hcp α (left) and bcc β (right) (Leyens & Peters., u.d., p. 4). The lattice parameters a (0.295 nm) and c (0.468 nm) are also indicated in Figure 2-2. The c/a ratio here is then 1.587, which is smaller than the hcp crystal structure ideal ratio, 1.633. The planes shown in the figure are the basal plane (0002), the prismatic planes $\{10\bar{1}0\}$ and the pyramidal plane $\{10\bar{1}1\}$. The close-packed directions are marked with a_1 , a_2 and a_3 . The direction of these axes is the indices $\langle 11\bar{2}0 \rangle$. In Figure 2-2 to the right, there is the BCC crystal structure. This is formed in titanium above the $882 \pm 2^\circ\text{C}$ line in pure titanium. The $\{110\}$ plane shown is just one of the six variations of the most densely packed lattice plane. The lattice parameter shown is $a = 0.332 \text{ nm}$ for 900°C .

2 Theoretical foundation and background

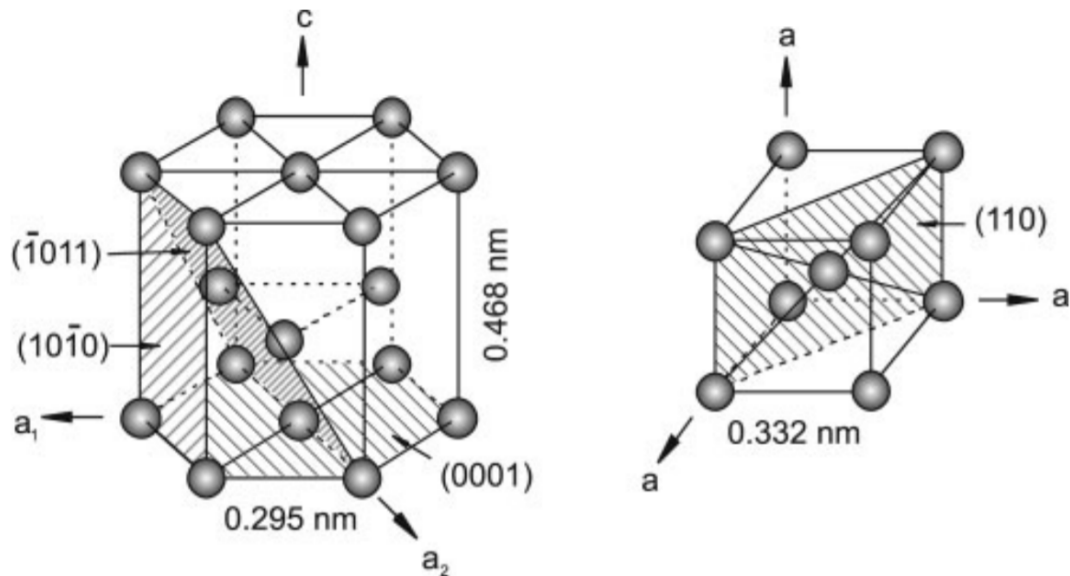


Figure 2-2 Crystal structure of hcp α (left) and bcc β (right) (Leyens & Peters., u.d., p. 4)

2.2 Direct metal deposition

Direct metal deposition (DMD) is an additive layer manufacturing or 3D-printing technology that adds layer on top of layer to form an object. In the case of Norsk titanium's patent, it uses a wire-based feed. There are two gas transfer arcs, one which heats up the deposition area and one to heating up and melting the wire. The patent, and machine itself allows to create freeform objects. One of the main the differences is that other DMD techniques uses a gas curtain. In which the gas is held inside a small compartment around the area where deposition occurs. In the NTiC patent, the base substrate and

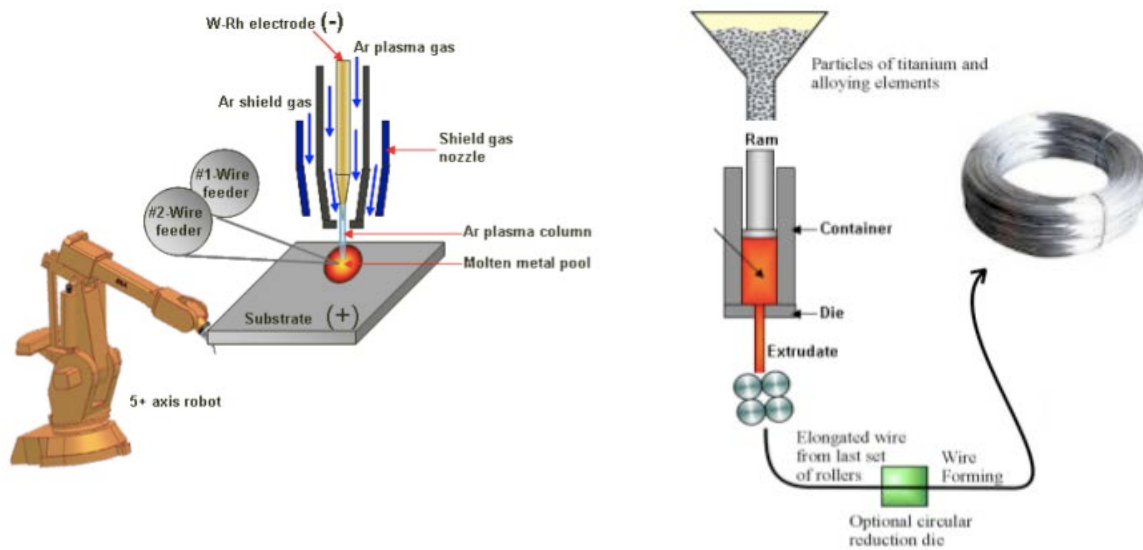


Figure 2-3 NTiC patent-Creating the wire from titanium particles and heating it with plasma (Norsk Titanium, 2010)

2 Theoretical foundation and background

deposition equipment is put inside a “house” which is filled with inert gas. The first plasma transfer arc is used to preheat the substrate base material and form a molten pool. The wire material is positioned above the molten pool and another plasma transfer arc (PTA) is used to heat the wire so that molten metallic material is dripping into the molten pool. The substrate is now positioned and moved in relative to the PTA in a manner that allows for solidification of the molten area. This fuses the layers on top of each other in the z-direction. Metallic bonds are formed between each layer and eventually a 3D object is made. NTiC uses a robotic arm from ABB which can be controlled by software. This method of manufacturing Titanium can make an object very close to specification. So that there is very little need for machining compared to forged or casted titanium. Seeing as titanium is a very expensive material, this is very cost-efficient way to manufacture parts. (Norsk Titanium, 2010). So it is important to keep a low buy-to-fly ratio (a term for which to create titanium as close to specification as possible to avoid machining). For each added layer, the base structure, or previous layer, is reheated to create a molten pool again. This type of solidification can be compared to welding and casting. (Stempfer, 2011)

2.3 Phase transformation

In titanium there are two main transformations. The first one is from above liquidus temperature of 1670°C when titanium is in the form of liquid metal. When the temperature goes below this temperature the titanium starts solidification and is completed when the titanium reaches the solvus temperature.

The second one is the allotropic phase transformation when the β -phase starts to transform into α -phase. This temperature at the β -transus line depends on the alloying material. For commercially pure titanium, only small parts of oxygen are allowed. Iron is considered an impurity. This combination sets the temperature for grade 2 at (**Error! Reference source not found.**Table 2-2) 915°C.

2 Theoretical foundation and background

2.3.1 Solidification

When the metal melt pool begins to cool down and the temperature reaches below 1670°C the solidification process begins. The initial size of the columnar grains is inherited from the base substrate. The sequential layer will gain grains with more favorable orientation. Welds with bcc types will develop sharp $\langle 100 \rangle$ solidification texture. The reason for this orientation is more favorable is that the

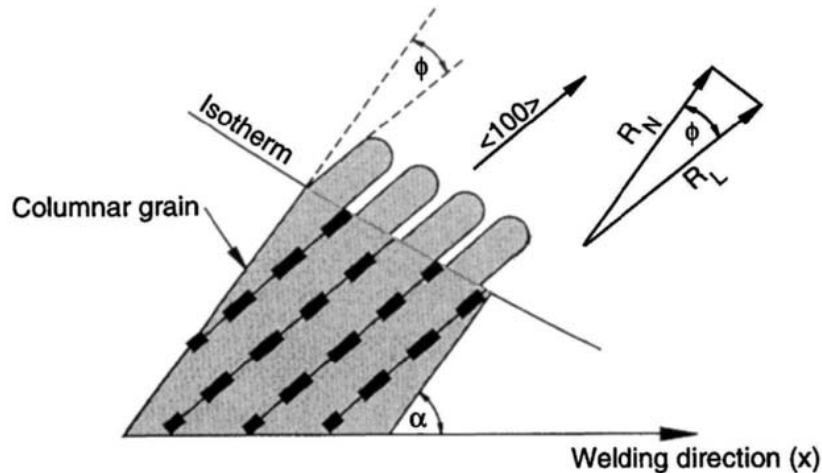


Figure 2-4 Solidification grain direction of welds (Grong, 1997, p. 236)

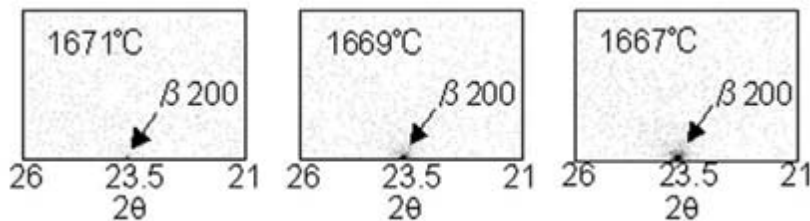


Figure 2-5 Observations of solidifications from liquid metal to β -phase (Yu-ichi, et al., 2009)

arrangement of atoms with low packing density has a lower energy configuration (Grong, 1997, pp. 226-237). An illustration of the grain growth is shown in Figure 2-4. Observations by this has been made and can be seen in Figure 2-5.

2 Theoretical foundation and background

2.3.2 Solid allotropic transformation from β to α and HAZ

During the cool down, the most densely packed planes of β -phase $\{110\}$ transforms to the basal plane in α $\{0001\}$. The slight difference in size of the planes causes a slight atomic distortion. This contracts the c -axis relative to the axis in hcp and reduces the a/c ratio below the ideal value for hcp atomic structures. The Burgers' orientation relationship (BOR) for the transformation of bcc β Ti to hcp α Ti is the following (Burgers, 1934):

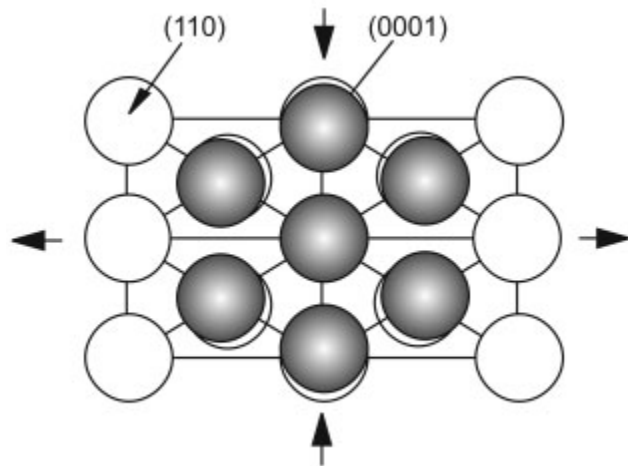


Figure 2-6 $\beta \rightarrow \alpha$ transformation according to burgers relationship (Leyens & Peters., u.d., p. 7)

$$\{0001\}_\alpha // \{110\}_\beta \quad \{1120\}_\alpha // \{111\}_\beta$$

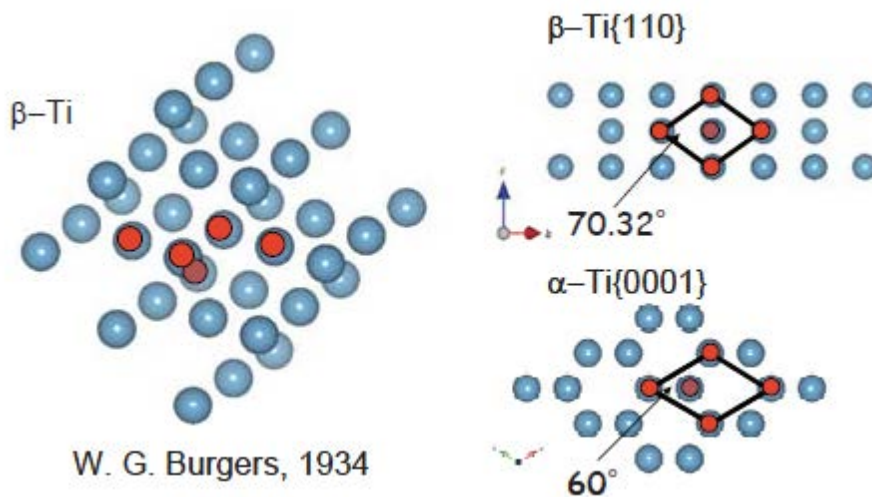


Figure 2-7 $\beta \rightarrow \alpha$ transformation in pure titanium (Yu-ichi, et al., 2009)

The transformation from β to α has also been shown to be very cooling rate dependent (Chun & Wen-feng, 2010). The study showed that cooling rates up to 15°C/s had some fine granular structured residual β phase turning into lamellar structure. The resulting microstructure shows that some β phase is retained in the α phase. This behavior increased as the cooling rate increased. While cooling rates lower than

2 Theoretical foundation and background

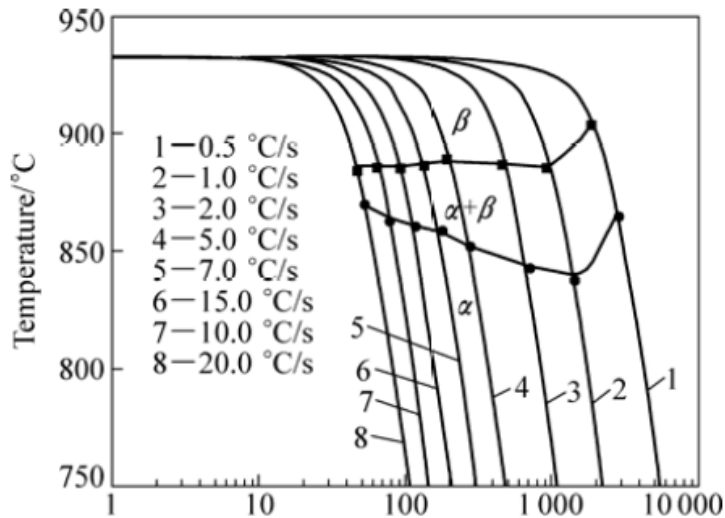


Figure 2-8 Dynamic CCT diagram for CP-Ti (Chun & Wen-feng, 2010)

15°C/s the microstructure mainly becomes lamellar α phase. The dynamic CCT diagram is showed in Figure 2-8. While 15°C/s is a critical turning point for β phase, the α showed different structure at lower cooling rates. For lower than 2°C/s, plate like α phase forms. At 5-10°C the α phase will show a serrated form. For cooling rates higher than 15°C/s gives the α phase a net-like appearance (Figure 2-9).

In the HAZ area around the metal melt there is a transformation from α phase back to β . In a study (ELMER, et al., u.d.) it is showed that the α to β in HAZ took place over a 285°C range (885-1170°C). Back to α took place over a 55°C (915-860°C). The study also note that the α to β microstructure is difficult to characterize since it is masked by the back transformation during cooling.

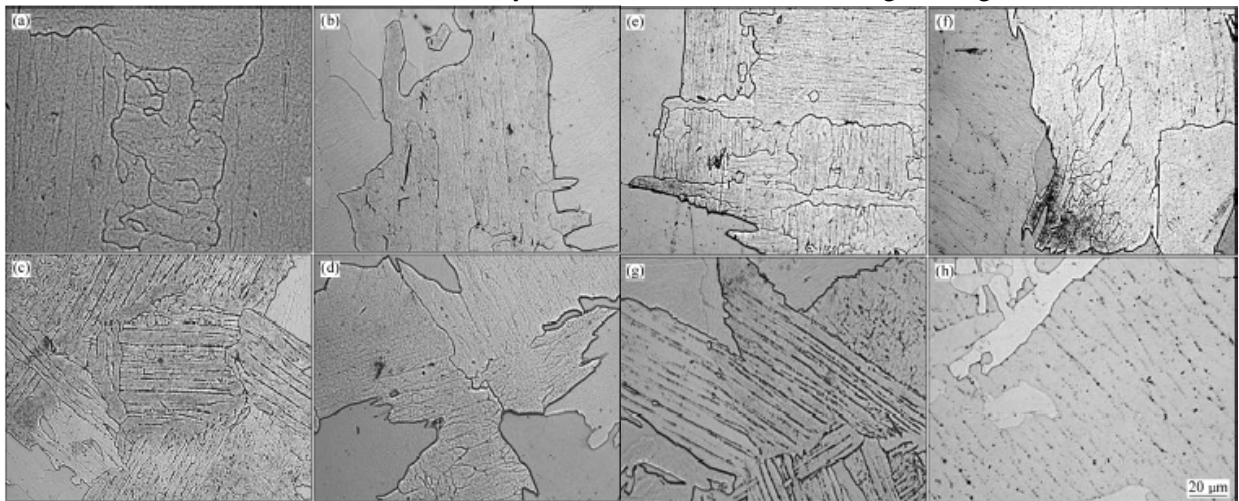


Figure 2-9 Optical micrographs of alloys at different cooling rates: (a) 0.5 °C/s; (b) 1 °C/s; (c) 2 °C/s; (d) 5 °C/s; (e) 7 °C/s; (f) 10 °C/s; (g) (Chun & Wen-feng, 2010)

2 Theoretical foundation and background

2.4 Deformation Modes

The hcp α -phase has a ductile behavior. Especially at low temperatures. This is because of the resulting activation of twinning deformation modes and slip by dislocation. In CP titanium, twinning modes are important for the deformation behavior. In two phase alloys like Ti-6Al-4V the twinning is nearly completely suppressed. This is because of the presence of TiAl₃ precipitates, small phase dimension and high solute content.

2.4.1 Slip modes and dislocations

Table 2-3 Deformation slip mode of hexagonal titanium

Slip mode	Plane	Direction	Multiplicity
Basal $\langle a \rangle$	{0001}	$\langle 11\bar{2}0 \rangle$	3
Prismatic $\langle a \rangle$	{10 $\bar{1}0$ }	$\langle 11\bar{2}0 \rangle$	3
Pyramidal $\langle a \rangle$	{10 $\bar{1}1$ }	$\langle 11\bar{2}0 \rangle$	6
Pyramidal $\langle a+c \rangle$ 1st order	{10 $\bar{1}1$ }	$\langle 11\bar{2}3 \rangle$	12
Pyramidal $\langle a+c \rangle$ 2nd order	{11 $\bar{2}2$ }	$\langle 11\bar{2}3 \rangle$	6

Slip systems are sets of slip planes and slip directions for where dislocation can most easily appear.

Generally slip appears in close packed planes. In Figure 2-10 there is an illustration on the various slip planes and slip directions. The main slip directions are the three $\langle 11\bar{2}0 \rangle$, these are close-packed directions. There are three different slip planes containing a burgers vector, (0002) plane, three {10 $\bar{1}0$ } planes and six {10 $\bar{1}1$ } planes. These form together 12 slip systems. The type of dislocation that can occur

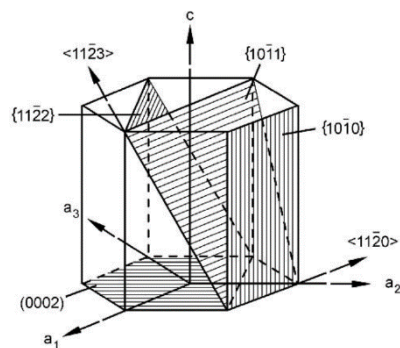


Figure 2-10 Slip planes and slip direction in hcp Ti (Lutjering & Williams, 2007, p. 20)

are edge and screw dislocation. There is also a mix between them. The most common slip system in hcp are the prismatic {10 $\bar{1}0$ }- and basal {0001}- planes with the burgers vector of $b=1/3\langle 11\bar{2}0 \rangle$. (Lutjering & Williams, 2007) The principal deformation mechanism in pure titanium have been established to be {10 $\bar{1}0$ }<11 $\bar{2}0$ > (WILLIAMS, et al., 2002)

2 Theoretical foundation and background

2.4.2 Dislocations

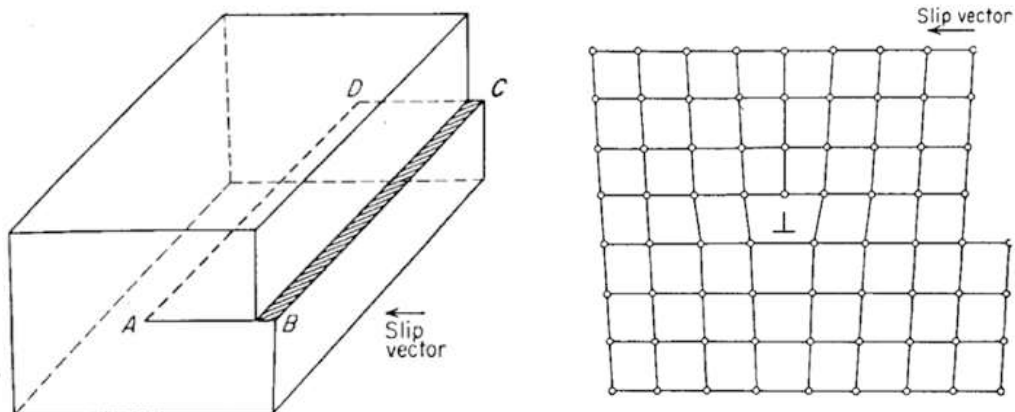


Figure 2-11 Edge dislocation occurs when slip vector is perpendicular to the AD slip line. (Dieter, 1986)

Line defects, dislocations that arise from the slip direction are edge, screw and a mix of them both. The defining parameters of dislocations, are the dislocation line, its glide plane, and its Burger's vector, b . In edge dislocations, the dislocation line is perpendicular to the slip vector. This can be seen in Figure 2-11. In the picture of Figure 2-11 it can be seen the movement of the area above the ABCD with the slip vector. The amount of displacement here is governed by the Burger's vector. Above the dislocation there will be an area of compressive stresses. Below the dislocation it will exhibit tensile stresses. It is possible for the edge dislocation to move perpendicular to its Burgers vector. This is called a dislocation climb. For screw dislocation, the slip vector is parallel to the dislocation line AD. Screw dislocations does not have a specific slip plane, which makes its movement less restricted. This means that the burgers

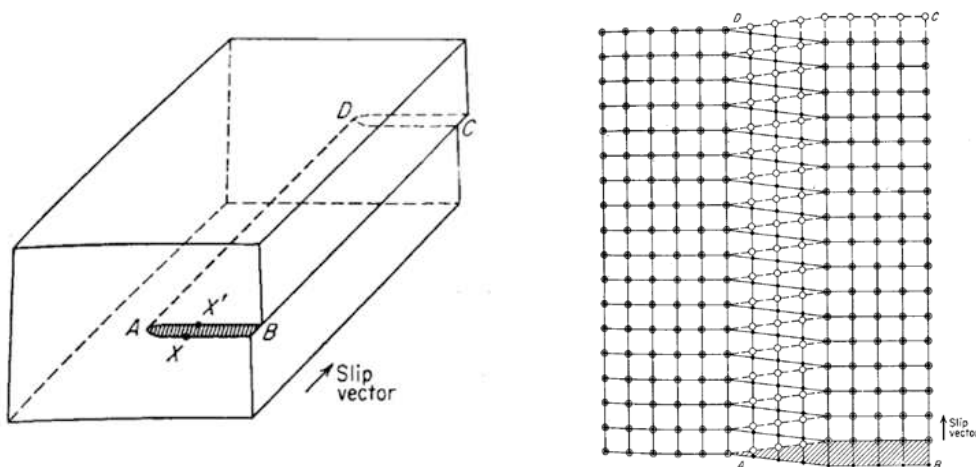


Figure 2-12 Screw dislocation with the slip vector going parallel to the dislocation line

vector of screw dislocation lies in parallel to the slip direction and is then $b = \langle 11\bar{2}0 \rangle$. In the edge

2 Theoretical foundation and background

dislocation the burgers vector is perpendicular to the slip vector and is $\mathbf{b}=\langle 0002 \rangle$. Unlike edge dislocations, it is not possible for the screw dislocation to climb.

Movement of the dislocation are possible. The plane which contains both the dislocation and the burgers vector is called the slip plane. For the screw dislocation, burger vector goes parallel to it. This means that any plane which has a screw dislocation is a possible slip plane. The screw dislocation may move by the action of slip, or glide in any direction perpendicular to itself. The edge dislocation is different because the burgers vector is perpendicular to it. This means that the edge dislocation only have one possible slip plane, and it can only glide in this direction, but edge dislocation there is also a

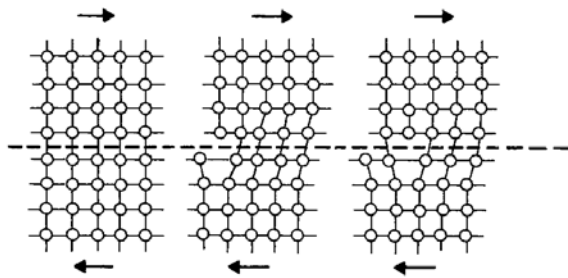
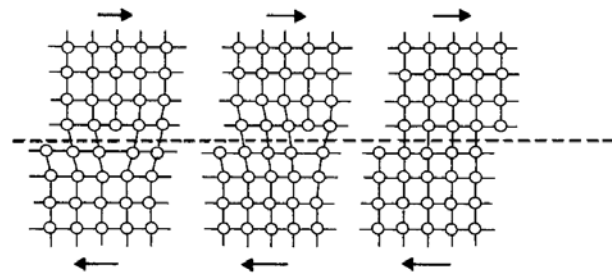


Figure 2-13 Schematic drawing showing the process of climbing for edge dislocation (Meyers & Chawla, 2009, p. 270)



fundamentally different type of movement. The edge dislocation can move perpendicular to its slip plane in a process called climb. Whereas slip occurs as a cause from shear stress, the climb happens because of normal stress. There are also movement in the intersection of the dislocation. When dislocations are moving in its slip plane it can encounter other dislocations moving in its slip plane. When a step lies in the slip plane of the dislocation it is called a kink. The other movement is when the step is taken normal to the slip plane of a dislocation, this is called a jog. (Abbaschian & Reed-Hill, 2011, pp. 104-105)

This thesis will use a criterion called the $\mathbf{g} \cdot \mathbf{b} = 0$ criterion. This means choosing a reciprocal lattice constant, \mathbf{g} , in the TEM. So that the dot product of $\mathbf{g} \cdot \mathbf{b}$ is zero. (KEHAGIAS, et al., 1994) and (Delimitis, 2018). This will effectively hide the dislocation type with corresponding burgers vector.

2 Theoretical foundation and background

2.4.3 Dislocation Density and its relationship to stress

Continued straining of the metal will result in increased number of dislocations. Increased concentration is closely associated with increase in strength and hardness of the material. In order to find this concentration there are two ways. The dislocation density, whose parameter is ρ , is found by measuring the total length of the dislocation lines in a unit volume. This requires that the volume is known, or more specifically, the thickness of the sample being viewed is known. The dimensions would then be defined as $\rho = \text{cm}/\text{cm}^3$. The difficulty here is to find the thickness as often not possible. An alternative way, is to not use the thickness. This way dislocation density is the number of dislocation per cm^2 , $\rho = N/\text{cm}^2$. (Abbaschian & Reed-Hill, 2011, p. 133)

Table 2-4 Collected from (Abbaschian & Reed-Hill, 2011) and (P.Rodriguez-Calvillo & J.M.Cabrera, 2015)

	Values	Reference
σ_0 for pure Ti	78,45MPa	(Abbaschian & Reed-Hill, 2011)
σ_0 for grade 2 Ti	283MPa	(P.Rodriguez-Calvillo &
k	3.69MPa $\text{mm}^{-1/2}$	J.M.Cabrera, 2015)
Length of b	0.34nm	
Shear modulus	45.6 GPa	

The relationship between the stress and the dislocation density is $\sigma = \sigma_0 + k\rho^{1/2}$. In this equation, σ_0 is the stress obtained when the root of the dislocation density is extrapolated to 0, $\rho^{1/2}=0$, and k is a constant. For the shear stress $\tau = \tau_0 + k\rho^{1/2}$ can be used. Seeing as if the dislocation density was zero, the material could not be deformed. Because of this σ_0 and τ_0 , is considered as convenient constants. Taylor proposed in 1934 a theoretical relationship between flow stress and dislocation density. This equation is $\tau = \alpha\mu b\rho^{1/2}$. Where μ is shear modulus. The length of Burgers vector, b . (Abbaschian & Reed-Hill, 2011)

2.4.4 Deformation twinning

Twinning modes are tension or compression in the c axis Figure 2-13. The most commonly observed twin modes in titanium are $\{10\bar{1}2\}\langle\bar{1}011\rangle$ extension twinning, and the $\{2\bar{1}\bar{1}2\}\langle 2\bar{1}\bar{1}3\rangle$ compression twinning. When the stress axis is parallel to the c-axis and the dislocations with a basal Burgers vector cannot move, the $\{10\bar{1}2\}$ and $\{11\bar{2}1\}$ are activated. This leads to an extension in the direction of the c-axis. Twinning as a general deformation only play a major role in low oxygen content of commercially

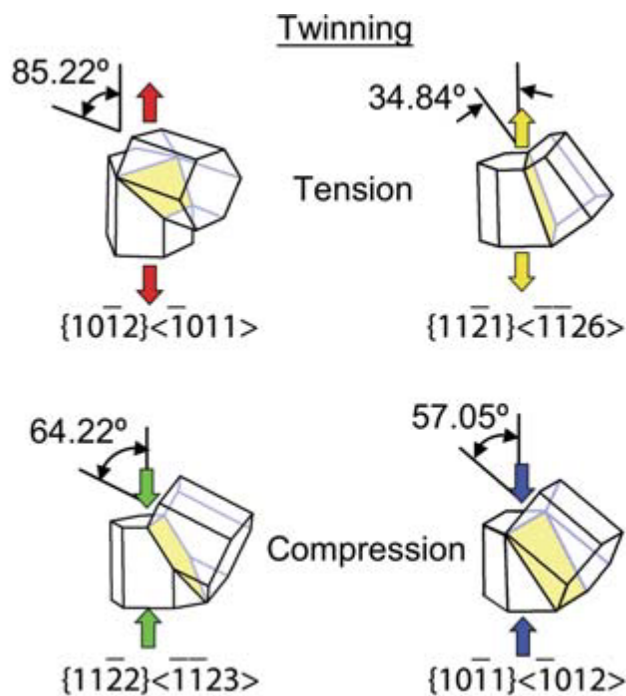
2 Theoretical foundation and background

pure titanium (CP-Ti) or in pure titanium. (Lutjering & Williams, 2007, p. 34) (Sinha, et al., 2017). Of the types of twinning deformation, only $\{10\bar{1}2\}$, $\{11\bar{2}1\}$ and $\{11\bar{2}2\}$ occur in room temperature. In Figure 2-13 there is a visualization of the angles for the twinning. When looking at misorientation between the grain boundaries these angles will show on twinning deformities. (PADILLA, et al., 2007). Of all the possible twin modes, the $\{10\bar{1}2\}$ twin gives the lowest shear. This is an obvious factor because of the universal observation of this mode. (Christian & Mahajant, 1995).

Table 2-5 Deformation twinning modes for hexagonal titanium (Nervo, et al., 2015)

Twinning mode	K_1	η_1	Angle-axis
Tensile twin 1	$\{10\bar{1}2\}$	$\langle\bar{1}011\rangle$	$85^\circ\langle 11\bar{2}0\rangle$
Tensile twin 2	$\{11\bar{2}1\}$	$\langle\bar{1}\bar{1}26\rangle$	$35^\circ\langle 1\bar{1}00\rangle$
Compressive twin 1	$\{11\bar{2}2\}$	$\langle 11\bar{2}\bar{3}\rangle$	$65^\circ\langle \bar{1}100\rangle$
Compressive twin 2	$\{10\bar{1}1\}$	$\langle\bar{1}012\rangle$	$54^\circ\langle \bar{1}2\bar{1}0\rangle$

Figure 2-14 Schematic view of the tension and compression twinning. Their angles according to the boundary misorientation is shown. (PADILLA, et al., 2007)



2 Theoretical foundation and background

2.5 EBSD

The electron backscattering diffraction detector is a detector that is made to increase the fraction of backscattered electron coming from the atomic planes of the surface of the specimen. It can be mounted to a free port of a regular scanning electron microscope (SEM). The detector provides quantitative information about the crystallographic nature of inorganic crystalline materials. It is used to

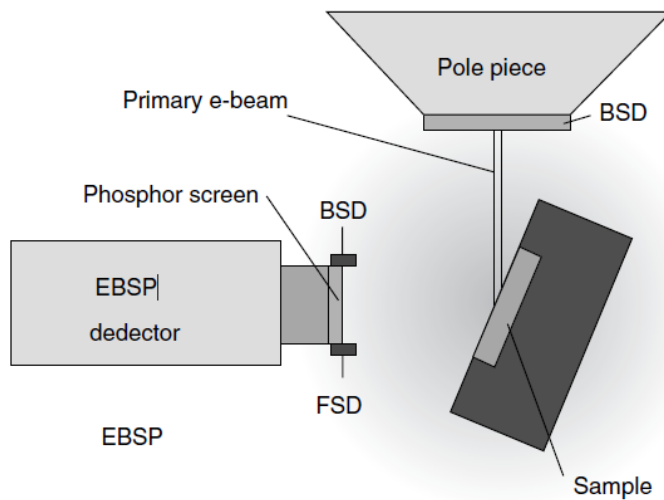


Figure 2-15 Schematic drawing of the SEM sample holder at tilt and EBSD detector (Zhou & Wang, 2006, p. 47)

explore microstructure and can reveal information like texture, phase identity, grain size, grain orientation and grain boundary. The nominal angular resolution limit is $\approx 0.5^\circ$. However the spatial resolution is related to the SEM itself. The sample needs to be tilted 70° from the electron beam, with a working distance of 5-30 mm. With the EBSD, it is possible to create a diffraction pattern. The primary beam interacts with the crystal lattice. From this interaction low energy loss backscattered electrons are formed. These electrons are channeled to a constructive and destructive interference pathway. This diffraction pattern can be analyzed over a wide area to give information from the sample which is otherwise hidden from SEM. The resulting Kikuchi bands is analyzed by using an optimized Hough transform. Using EBSD to create an orientation image microstructure (OIM) has become a common method for studying microstructure. (Zhou & Wang, 2006, pp. 41-51)

2 Theoretical foundation and background

2.5.1 Inverse pole figure

The inverse pole figure (IPF) is made together with an EBSD mapped image to show the different orientation. Often included as a legend. It gives a visual information and color coding to various crystal orientations. In Figure 2-15 there is an example of an inverse pole figure. The visual representation shows which color corresponds to which orientation. (Zhou & Wang, 2006, pp. 57-58)

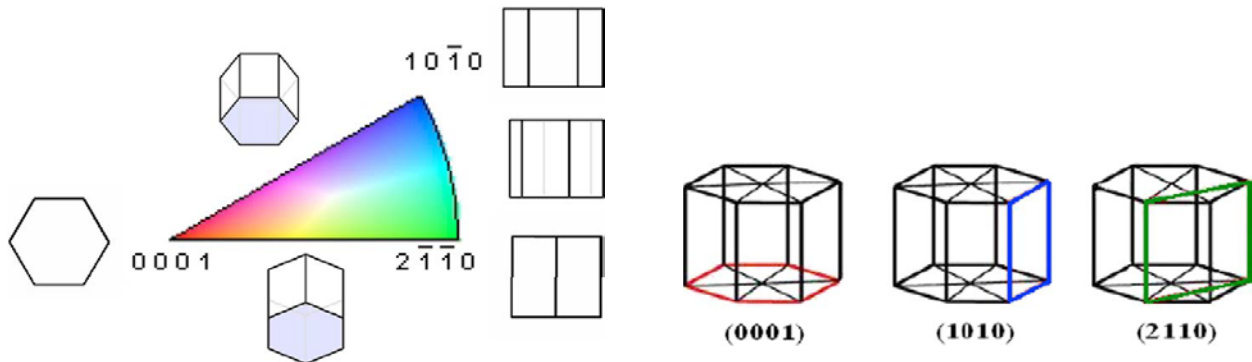


Figure 2-16 An example of an inverse pole figure (Vera, et al., 2017)

2 Theoretical foundation and background

2.6 TEM

Transmission electron microscope is a type of microscope that uses electrons instead of light. Much like SEM. The major difference in the TEM is that compared to the SEM which sends electrons and detects the information coming back. Visible light has a minimum wavelength of about 400nm, electrons have 0.0251nm for a 200kV TEM. This leads to orders of magnitude higher theoretical resolution. The TEM sends the electrons through the sample, and is detected on the other side. This means that the sample

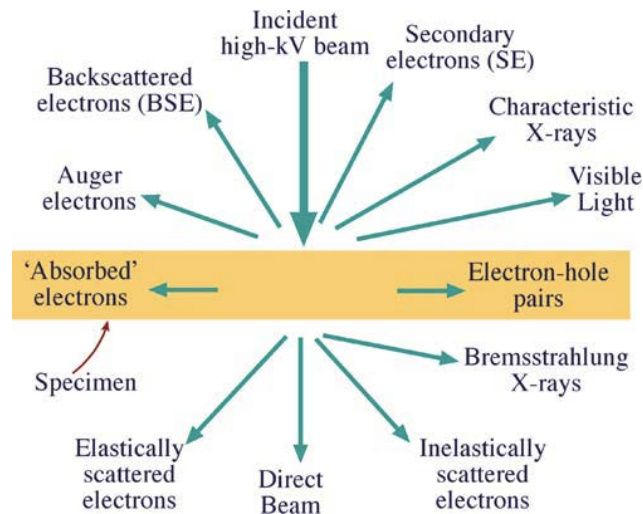


Figure 2-17 The various electron incidents reacting from central beam (Williams & Carter, 2009)

must be sufficiently thin in order for the electrons to pass through, seeing as solid materials are highly absorptive. Figure 2-16 shows the different reaction electrons have and the difference in the information SEM and TEM can obtain. Instead of having optical lenses, the lenses used in TEM are of the electromagnetic ones. These lenses form the image that is sent to a fluorescent screen on which an image is formed. When the electrons hit the specimen they are scattered. When the electrons scatter by the nucleus in a single direction they can fulfill Bragg's law. The interference of these patterns form a diffraction pattern. Center spot of a diffraction pattern is the direct beam, and the spots are called reflections. These patterns can be indexed and to know which plane the image which is viewed is from. (Williams & Carter, 2009, pp. 3-15) (Shindo & Oikawa, 2002, pp. 1-19).

2 Theoretical foundation and background

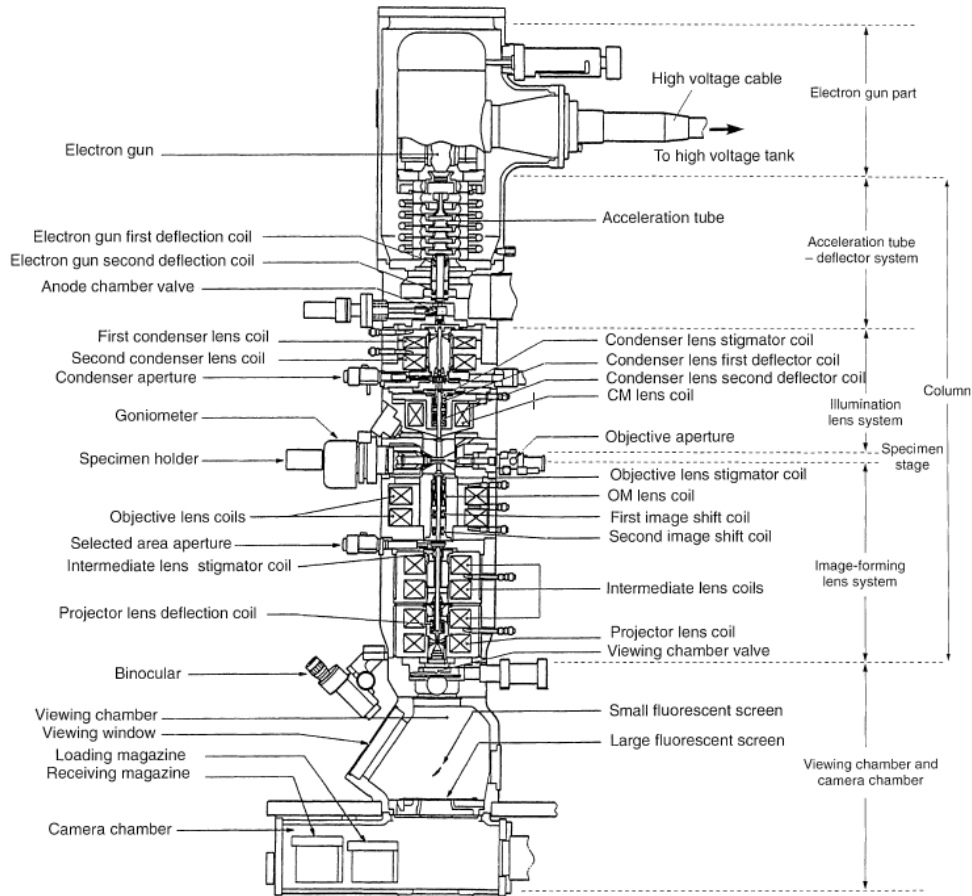


Figure 2-18 A cross section view of a column in TEM (Shindo & Oikawa, 2002, p. 15)

3 Experimentation

3 Experimentation

In this chapter I will go through the various steps in the experiments carried out. The preparation steps taken for each of the experiments are explained. The experiments carried out is chemical analysis, EBSD and TEM. The reason for a chemical analysis is carried out is to discover the actual content of iron (Fe) since Fe is treated as an impurity, or other elements what will change the phase transformation. The EBSD experiments is used to discover general grain size, eventual deformation, and from the thick sample. It is interesting to see if there is a morphological difference between the inside non-machined part, compared to the middle of the sample and the outside machined edge. The TEM experiment is to discover dislocations, general direction of dislocations, quantity, and even to try to measure the edge to screw dislocation ratio. In many preparation studies of Ti, hydrofluoric acid (HF) is often used. But because of HMS regulations and the general dangers of this material most places which used HF have now foregone the use of it. UIS laboratories and company laboratories have stopped the use of this acid.

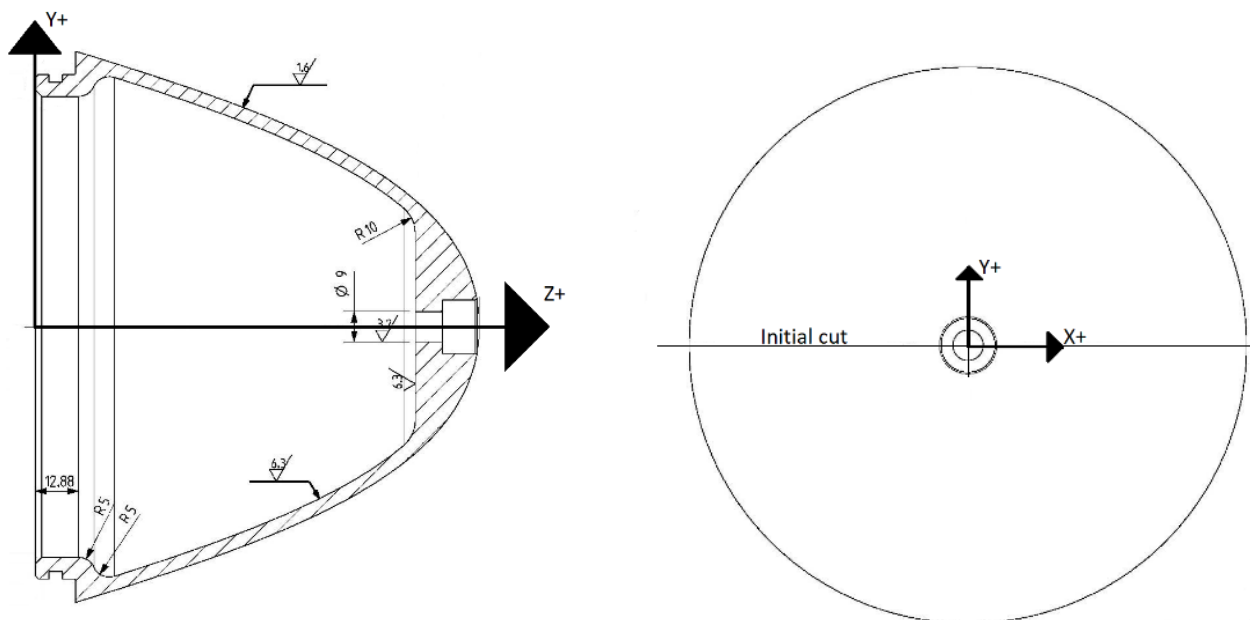


Figure 3-2 Side view of the specimen it set to be the plane YZ

Figure 3-1 Top view of the sample is set to plane XY and the initial cut direction is in X direction

So in this thesis I will circumvent the use of HF. In general in this thesis, a non-HF based electrochemical polishing will be used for both the EBSD samples and TEM samples.

Establishing a coordinate system is imperative for orientation of samples. In Figure 3-2 and Figure 3-1 the planes and global coordinate system is shown. Samples will be named according to which plane they are taken from.

3 Experimentation

3.1 Preparation

The samples preparations are for three different techniques. The planes needed to be viewed is the XY plane and the YZ plane. Most samples will be in the XY plane. For the TEM, the samples need to be thin enough for the plane not to matter. For EBSD, the samples can be larger, and so the plane matters. For the regular VLM experiment, only the general structure is needed to be obtained. This is to visualize and compare to the cooling rate study (Chun & Wen-feng, 2010) to give a general understanding of what the



Figure 3-3 - Finished product made from DMD given by Norsk Titanium (right) and the cut line (right) from top of cone

cooling rate in the case for this DMD technique is. To give a better understanding of the solidification nature. The samples from EBSD can be used here. The samples looked at for the VLM are in the XY plane of the specimen. Both planes can be viewed, but the purpose of this experiment, only the general structure is needed to be viewed to compare it.

In order to view the samples with any technique, an etchant needs to be chosen and used. Instead of using an etchant containing hydrofluoric acid (HF), a specific type of electrochemical polishing will be used. The samples will be same size as the TEM sample, only thicker. Small circular discs with 3mm diameter are to be extracted.

The areas that will be studied are from the thick sample which is made by using two wires. Are the inner area, closest to the non-machined surface. The middle area, and outer area, closest to the machined surface. These are taken from the XY plane. From the thin sample, a sample taken from ZY plane, and in the XY plane. From theses samples, the grain size, boundary and general morphological nature is to be studied. Detect any presence of twinning and detect any presence of β -phase.

The TEM samples follow the same shape and size as for the EBSD, but are to be thinner and containing a hole with a thin enough region to be studied. The object to be studied here is the dislocation nature, quantity and direction. With a technique called a weak beam image, with the right zone axis, it is also possible to quantitate and measure ratio of edge to screw type dislocations.

3 Experimentation

3.1.1 Cutting

The samples given from Norsk Titanium can be seen in Figure 1-1. This were cut before the start of this thesis along the middle, as you can see in Figure 3-1. From this half dome a new cut was made roughly 1,5cm into the half dome. The resulting parts of this cut can be seen in Figure 3-6. The specifications for the complete component can be seen in Appendix A. The shape can be seen in Figure 3-3 and Figure 3-4. There were two samples given. One built with exact shape specification and machined on the inside and

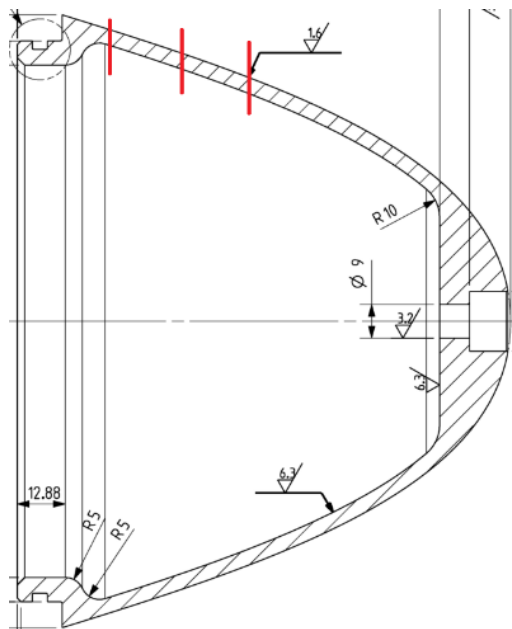


Figure 3-4 – Cross section view of the sample. The red lines corresponds to the cuts that were made during preparation. Similar cuts were taken in both the thin and thick sample, which were made by single and dual wire respectively.

outside. And one which is only machined on the outside. Pieces were then cut with Struers discotome 5 cutting machine with struers abrasive disc type 20s25. The cuts are visualized in Figure 3-4 with red lines. Lubrication used in the discotome is water. The feed rate was kept very low, at around 0,2-0,5mm/s. The discotome had a sensor which indicated workload, and heat propagation. To keep this sensor low, the feed rate was kept low as well. The sample pieces needed to be thin enough to be electrochemically polished. To achieve thin cuts needed for both SEM and TEM preparations the samples needed to be cut by struers accutom. Feed rate was set sufficiently low, around 0.1mm/min. For a sample size with the area 4mmx15mm it took about 45min. A very low thickness is needed here, so it was cut to <0.5mm. The cuts were made parallel to the red lines in Figure 3-3, and perpendicular, between two lines. The thin samples are then added on a plexiglass plate with strong double sided tape for easier grinding and polishing.

3 Experimentation

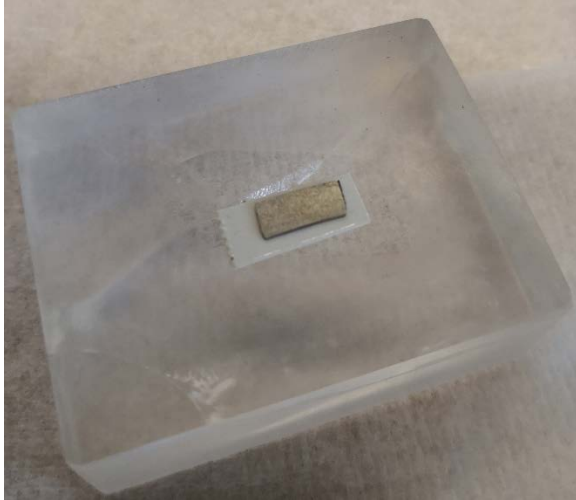


Figure 3-5 Thin sample mounted on plexiglass with the use of double sided tape for easier handling in grinding and polishing

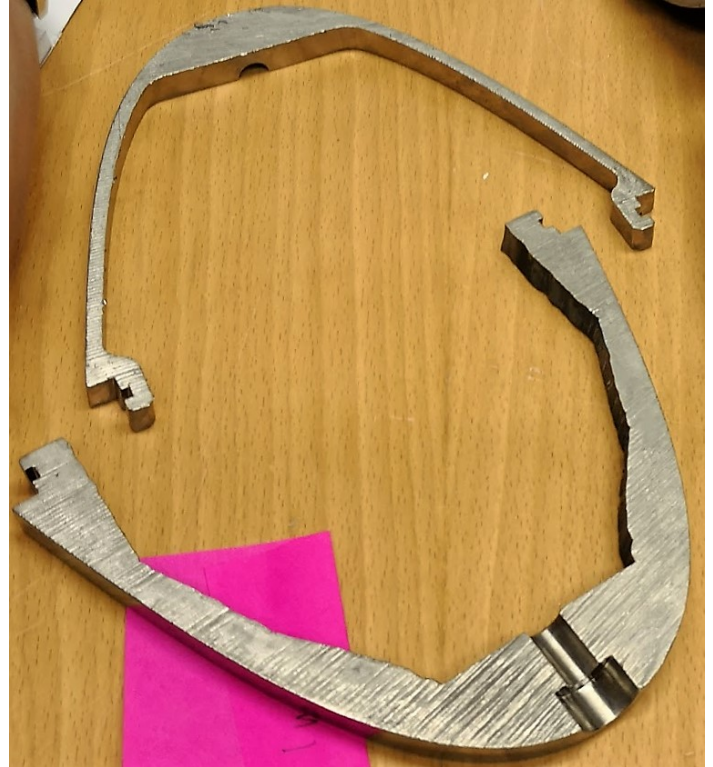


Figure 3-6 Finished cut samples of both the thick and thin

3.1.2 Grinding and polishing

Table 3-1 Grinding steps for EBSD and TEM samples

Step	Grinding surface	Time	RPM	Lubrication/suspension
1. Coarse	#220 SIC paper	Until plane*	300	Water
2. Coarse	#320 SIC paper	2 min	300	Water
3. Fine	#1000	8 min	300	Water
4. Fine	#2000	12 min	300	Water

*Step 1 can be skipped if cut is sufficiently plane. If not use maximum 2 min. If cut is very thick >1mm use more.

The thin samples which is now mounted on to the Plexiglas needs to manually be held steady in the grinding machine. For this set up the thin samples need to grinded on both sides, and sufficiently thin to be mounted into the electrochemical polishing mounting bracket. The steps for grinding the EBSD and TEM samples can be seen in Figure 3-2. Step 1 can be skipped if sample is cut sufficiently thin and plane. Extra precaution were taken when grinding with coarse paper as it would easily rip the sample from the

3 Experimentation

tape, and could also grind through the sample. When the samples have finished the grinding steps. The Plexiglas plate together with the sample mounted on it are submerged in liquid nitrogen. The double sided tape will freeze and release the sample. The sample is now flipped and attached on to the Plexiglas plate leaving the other surface exposed. The grinding steps 2-3 is repeated from Table 3-1 Grinding steps for EBSD and TEM samples and the steps 3-4 are prolonged to reach the necessary thickness for each sample. For EBSD samples, the electrochemical polishing is replacing etching with HF. These samples only need to fit inside the mounting brackets of the electrochemical polishing machine. For the TEM samples, they need to be sufficiently thin so the electrochemical polishing creates a hole in which we can use to study with the TEM. When the sample is thin enough they were cut with a special hole puncher for TEM discs, to create circular discs of 3mm diameter. From the thick sample, which were cut along the middle red line from Figure 3-3. 2 disks were made from the inside, near the edge. 2 more from the middle, and 2 from near the outside edge. Disks were also made from both samples from parallel and perpendicular angle according to the red lines in Figure 3-3. It is recommended to make more samples than what is needed as the electrochemical polishing can go wrong, and it is not possible to retry electrochemical polishing.

3.1.3 Electrochemical polishing

For EBSD the samples are prepared with electrochemical polishing after the grinding. A mixture of 59% methanol, 35% butan-2-ol ($C_4H_{10}O$) and 6% perchloric acid ($HClO_4$). This method is tested (Tirrya, et al., u.d.) to make sure no twins are introduced. The circular disk samples are mounted into the holder for the electrochemical polishing machine. The potential was set to 28V, and polished for 6 min. The temperature was set on $-40^{\circ}C$. The time and voltage was tested to find the best combination and the result gave best pictures for 28V at 6min. For the TEM samples, holes needed to be made. This is so there are thin enough regions on the sample for which the electrons of the TEM can be sent through. When a hole is made, the edges are usually thin enough and more easily studied in the TEM.

3.2 EBSD

The samples need to be on a conductive surface. They are placed on a metal holder, with conductive tape. For EBSD a special holder, which is able to hold the samples at a 70° angle from the electron beam. Finding the sample and focusing is a little different from regular SEM. When the sample is tilted, this means that the area of focus is only a small part of the sample at a given time. So in order to counteract this, the machine has a function called dynamic focus. With this, focus in the middle height of the area in question, and then adjust dynamic focus. Dynamic focus is given in %, so adjust this % until all of the

3 Experimentation

area is in focus. Once the image is formed, the EBSD programs can scan the diffraction patterns. 20kV with a stepsize of 0,6 μ m was used.

3.3 EDS experimentation

The thin samples is mounted in the holder and inserted into the TEM. At first the chemical composition is to be studied. It is important with cp-Ti as Fe is treated as an impurity. Since the specifications for the titanium used is known before manufacturing, we can compare the chemical composition for the finished part. This chemical study is carried out with TEAM EDS software.

3.4 TEM

TEM Using the sample already mounted in the machine of the TEM, from the previous step. The samples can be studied. Location of areas that is suitable for studying can be found near the hole by the electrochemical polishing. Focusing and tilting can reveal this areas, and give information like dislocations, grain boundaries and other deformities. Together with the diffraction images it is possible to know the zonal axis and what type of reflections being studied.

Using a few TEM techniques it is possible to reveal more information on the substructures. In the diffraction pattern, there is a center beam. Having this in the objective aperture focus is called a bright field (BF) image. The other spots are reflections and diffracted beams. Choosing with the objective aperture to focus on a diffracted spot gives a dark field (DF) image. This can be seen in Figure 3-7. This

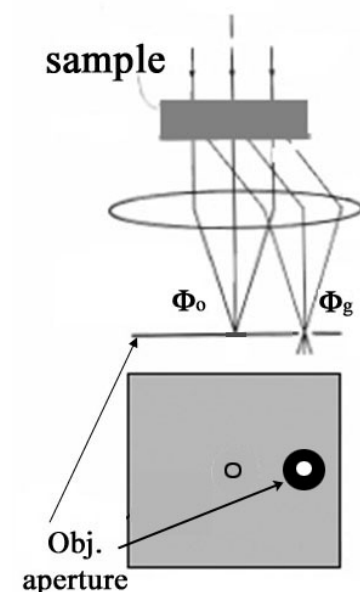


Figure 3-7 Choosing a diffraction beam with the objective aperture creates a dark field image

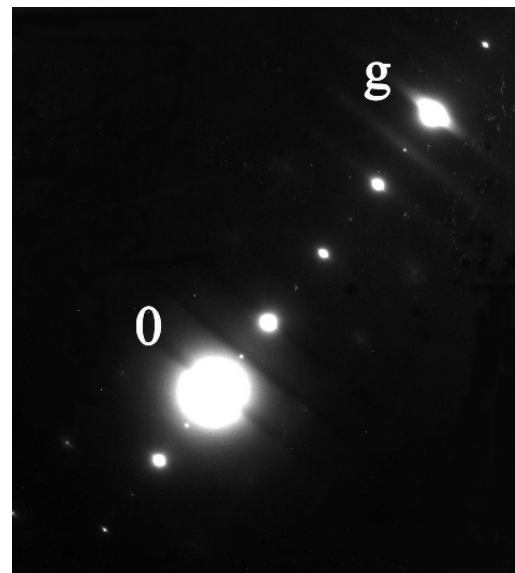


Figure 3-8 Forming two beam condition with center beam and a reflection, g

3 Experimentation

image is complementary to the bright field and gives information on the reflected beam. The DF image can give information on the information on the different crystallographic regions or phases.

DF imaging can also help in identifying some structural defects. When tilting in both direction, it is also possible to find a two beam condition. This is when two beams are focused and bright. This can be seen in Figure 3-8. On axis image often have too much information. So to use two beam condition lattice defects analysis are greatly facilitated. Two beam condition is a prerequisite for the weak beam imaging technique. Weak beam imaging is a DF image, when you choose a diffracted beam. With two beam condition forming having two strong beams. One center beam, and one of the reflections (g) forming a strong beam, seen in Figure 3-8 and Figure 3-9. A weak beam (WB) is when the beam opposite of the

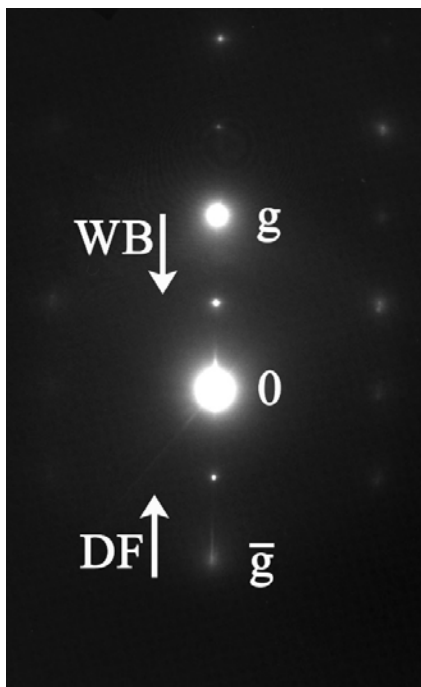


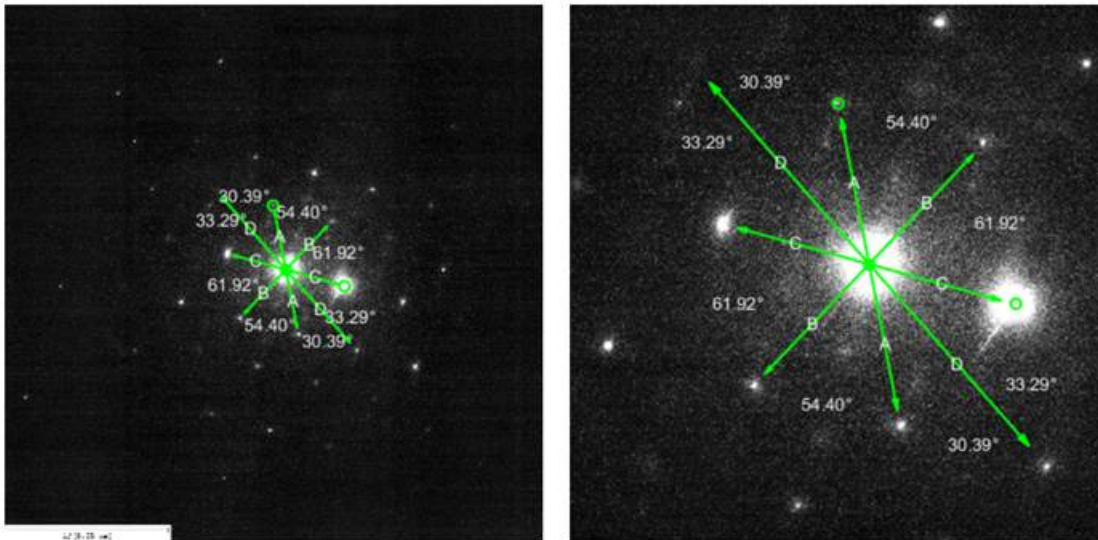
Figure 3-9 Diffraction image with a two beam condition formed. With the reflection g forming two beam. Moving the opposite, the $-g$, into the objective aperture forms a weak beam image.

reflected strong beam, $-g$. As the opposite reflected beam is moved towards the objective aperture, it will become stronger. This excludes the direct beam and all other reflections. This gives a higher contrast and makes it easier to identify structural defects.

Using the $\mathbf{g} \cdot \mathbf{b} = 0$ criterion it is possible to exclude some structures. During the TEM procedure, it is possible to choose a reciprocal lattice vector, \mathbf{g} , in a specific reflection so that we can exclude certain structures. The prerequisite here being that the diffraction image is indexed while doing the procedure. Screw and edge dislocations have their own burgers vectors, and choosing the perpendicular vector, the dot product would be zero. For edge dislocation in hcp the vector is $\langle 0001 \rangle$ and for screw dislocation it is $\langle 11\bar{2}0 \rangle$. Choosing a reflection with $\langle 0002 \rangle$ would form an image with no screw dislocations and

3 Experimentation

forming an image with $\langle 01\bar{1}0 \rangle$ would form an image with no edge dislocations. A dislocation can either be edge, screw or a mix of both. So when forming a WB image with one of these zeroed means we can



d-spacing	
	[nm]
A	0.12185
B	0.11996
C	0.13222
D	0.074618

d-spacing (Cal.coef.=1.06)	
	[nm]
A	0.12917
B	0.12715
C	0.14015
D	0.079095

d-spacing ratios [-]			
	A	B	C
A	1	1.0158	0.92161
B	0.98443	1	0.90726
C	1.0851	1.1022	1
D	0.61235	0.62204	0.56435

Figure 3-12 Indexing done by using Crystbox. The d-space is measured and given. In order to successfully index the d-spaces, angles and ratios must be analyzed and compared to known zone axis' like the one in Figure 3-11. Which matched this one.

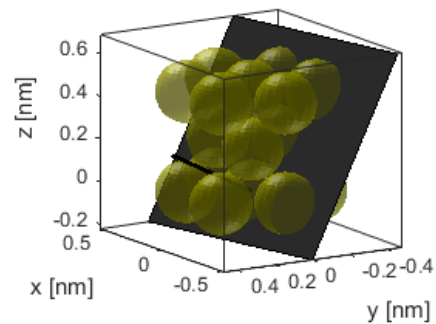
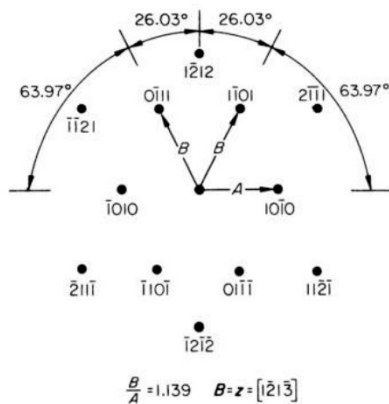


Figure 3-11 Zone axis of $[\bar{1}\bar{2}\bar{1}\bar{3}]$ that matches the d-spacing, ratios and angles to the one in Figure 3-12 (Edington, 1975, pp. 102-103)

Figure 3-10 Visualization of the $[\bar{1}\bar{2}\bar{1}\bar{3}]$ plane

calculate one ratio. When one type of dislocation is hidden, measuring the density of the rest. The amount of the dislocations that are gone is equal to the dislocation type hidden.

3 Experimentation

After the diffraction images are taken. It is time to index them. This is done by measuring the distance between the dots, and the angle between them. There are several tools in order to facilitate this type of work, but it has to be manually checked and verified. In Figure 3-12 there is an example of the indexing done. The scalebar is used to measure the pixel to nm scale so the program can measure correctly. Using these measurement and comparing the d-spacing (distance between spots), the angles, and the ratios, to known zone axis'. Figure 3-12 shows much the same characteristics as the zone axis of $[\bar{1}\bar{2}\bar{1}\bar{3}]$. The image and values in Figure 3-12 can be compared to the Figure 3-10 and Figure 3-11 where the zone axis is $[\bar{1}\bar{2}\bar{1}\bar{3}]$. This give information on where in the crystal lattice diffraction image is taken. It also gives you plane of orientation when discussing the different reflection from the spots which is also the different vector directions.

4 Results

4 Results

The results are divided into each experiment. Analyzing of the pictures will be done for each segment, and discussion and eventual conclusion will follow in the corresponding chapter. The results are focusing on mostly the EBSD and TEM.

4.1 EDS

The EDS results are gathered from the TEM machine. Considering the Ti sample, the only substances we should be able to find are Titanium itself, with maybe small parts of oxygen and iron. There might be some particles left from the polishing. In the manufacturing process, since it is made in an inert gas atmosphere, there should not be more oxygen than the original Ti used. From Figure 4-1 there is a clear corresponding case which matches the data for grade 2 Ti. The EDS spectra taken was mostly in this

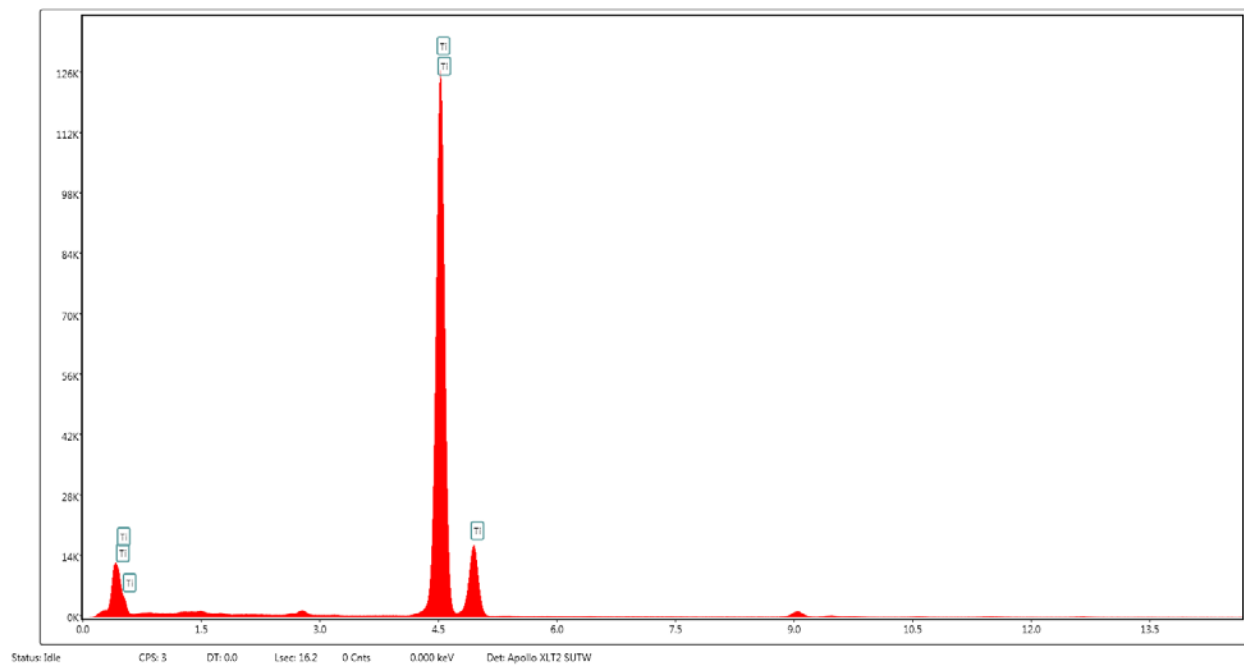


Figure 4-1 EDS spectra pure titanium

spectra. The levels of oxygen is hard to read here since the energy levels of Ti is similar. The oxygen energy reading can be seen in Figure 4-2 where it is more prevalent. Taking sample around the specimen it is also possible to find some other particles like Al and Cl. This can be seen in the EDS results from Figure 4-2. The Cl atoms are most likely from the perchloric acid (HClO_4) from the electrochemical polishing. The aluminum is not introduced from the experiments carried out from this thesis. As mentioned in 2.1.1 Crystal structure of titanium, Al is a α -stabilizer and should help stabilize the α -phase of the region it is present. Some regions also had elevated levels of oxygen, these regions also contain

4 Results

Cl, and could possibly be from the perchloric acid as well. The chemical composition of grade 2 Ti contain a maximum of 0.25% O. From sampling 10 areas with EDS it was discovered that 9 followed the archetype EDS from Figure 4-1. One area contained the EDS spectra from Figure 4-2. There was nothing morphologically different in the area taken from Figure 4-2. No Iron was found. There was one area which was found to contain Mg. Mg is neutral when it comes α or β phase. For the purpose of this experiment it is treated as an error, as machine error or contamination. Mg was not found except for the one spectra. This EDS is available in Appendix C.

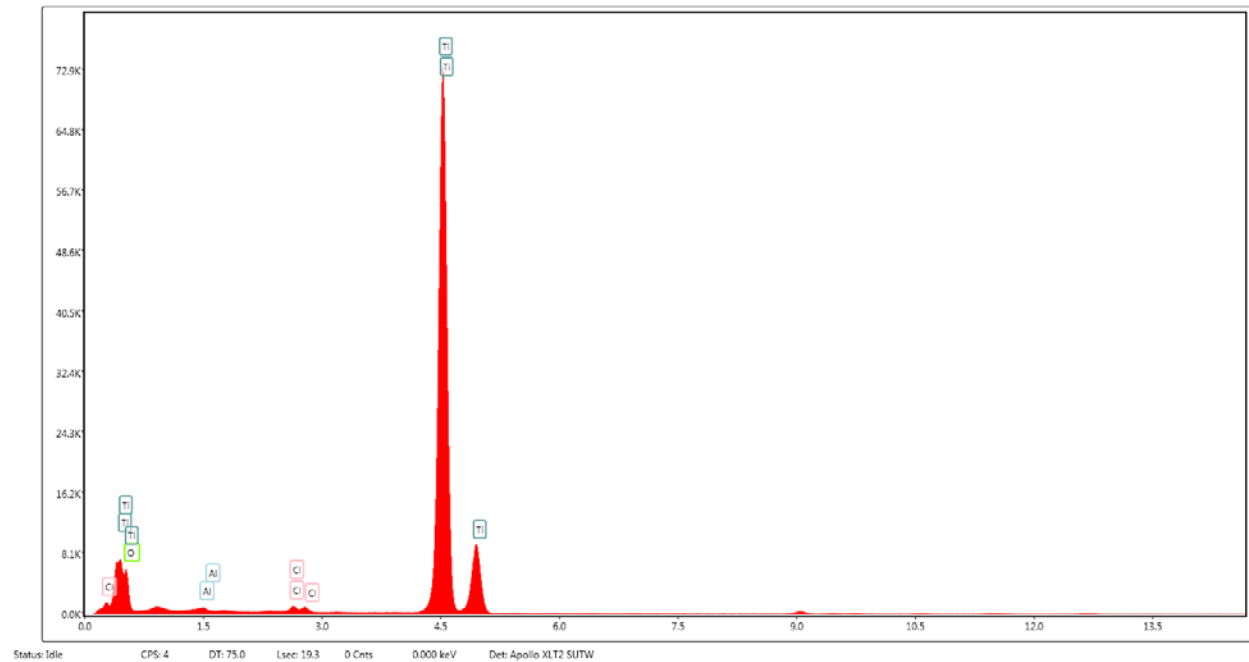


Figure 4-2 EDS containing elevated levels of Al, Cl and O

4 Results

4.2 Visual light microscope

The object of this is to give a visual representation for the material. Visual light microscope give a structural overview. It gives information on the Ti with a lower magnification so the general structure

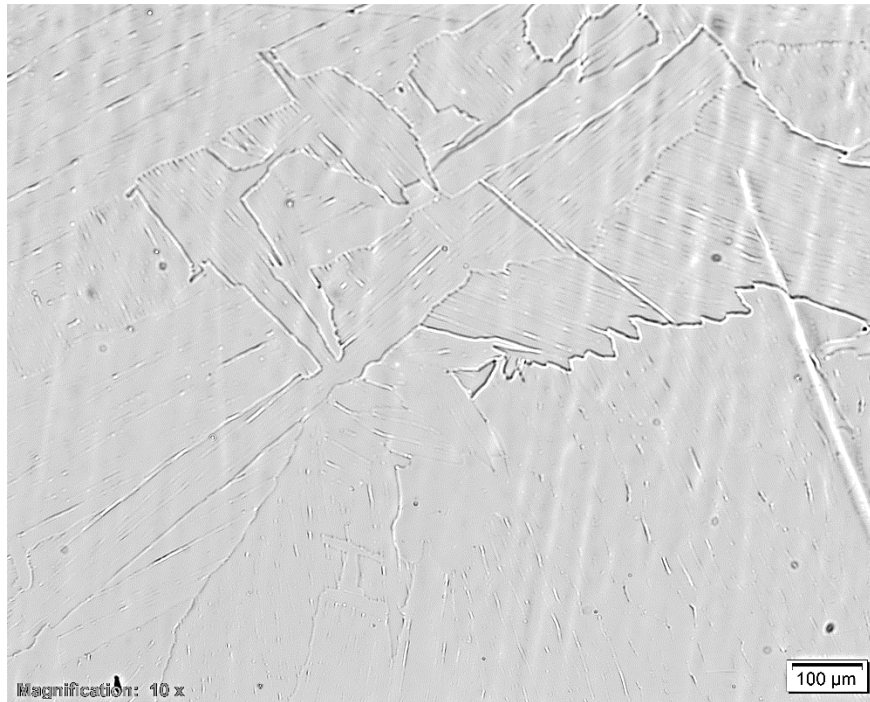


Figure 4-4 VLM picture from the sample. A general idea of the microstructure is needed to compare the pictures to study from the cooling rate. The etchants are different so edges might look different.

can be ascertained. From the Figure 4-3 it is possible to see hard edges. At lower cooling rates there would be softer edges between the grains. According to the cooling rate study (Chun & Wen-feng, 2010) and Figure 2-9 it resembles a cooling rate of 15°C/s. It does not look serrated, and the structure at 20°C/s would leave the α -phase serrated. Being close, or even over the critical point of 15°C/s means

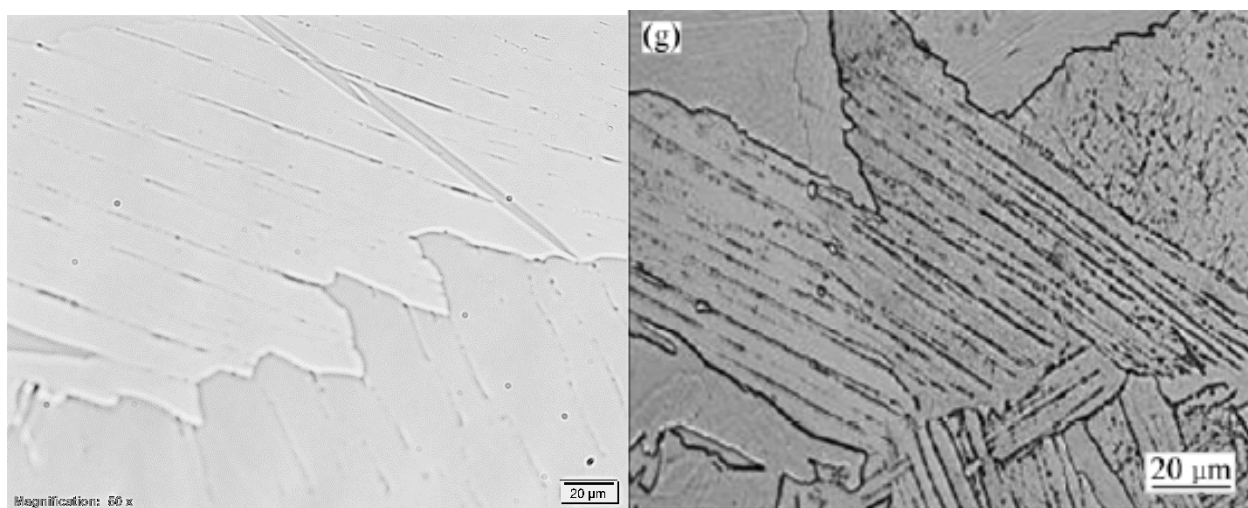


Figure 4-3 Comparison of the sample to the study of cooling rates (Chun & Wen-feng, 2010). The etchants used here are different, but comparing the different microstructures made this picture the best comparison. The picture to the right is the picture with 15°C/s. What to look for here is the sharp edges in the grains, and the lines in the grain themselves. This might lead to the possibility that the sample contains retained β -phase because of cooling rate.

4 Results

that there might be some retained β -phase that is the result of this cooling rate. This picture was taken from the thin sample, parallel to the XY plane. The point of VLM is to see if the structure had comparable high enough cooling rate to leave some β -phase.

4 Results

4.3 TEM

In the TEM the pictures were mostly focused on dislocations. Good pictures with dislocations are needed if quantification is to be performed. The images are taken from the thin sample, parallel to the base

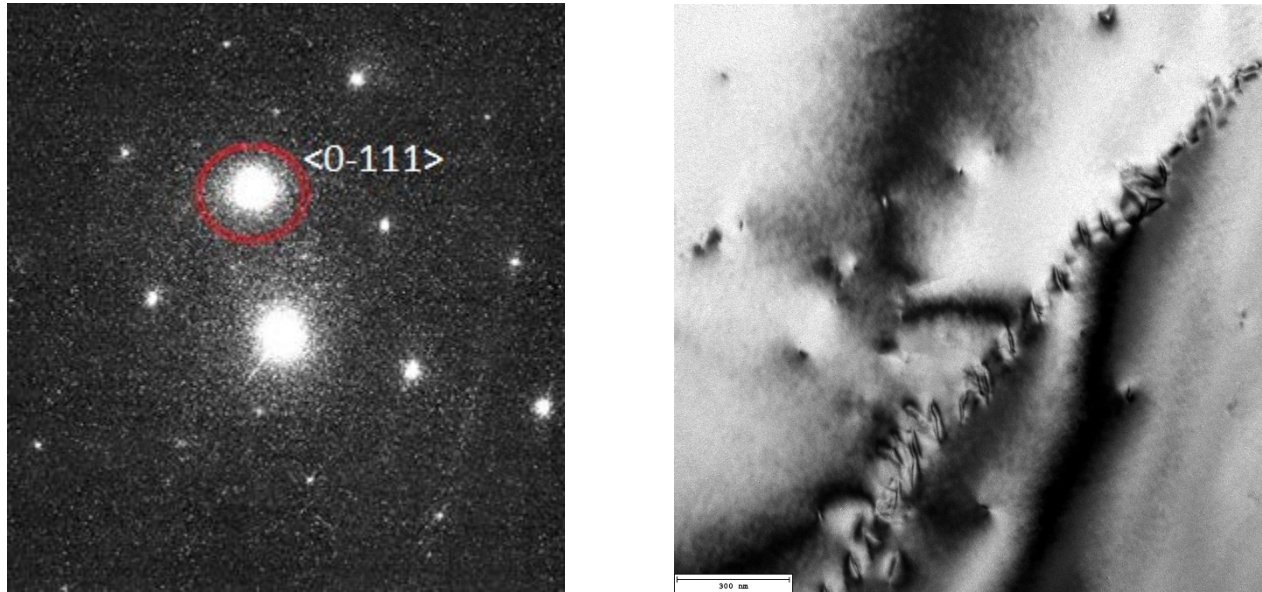


Figure 4-5 Diffraction image with its corresponding BF image. Zone axis here is $[\bar{1}\bar{2}1\bar{3}]$. The reflection chosen for WB imaging is marked with red $\langle 0\bar{1}11 \rangle$

plane. The images in Figure 4-5 shows a diffraction image with zonal axis of $[\bar{1}\bar{2}1\bar{3}]$. The corresponding BF image to this diffraction image shows that it is difficult to see the different dislocations showing. The red circle in the diffraction shows which reflection is chosen to best show the dislocations, this reflection is $\langle 0\bar{1}11 \rangle$. From Figure 4-7 the dislocations are visible and circled. In total there are 46 dislocations. Most of the dislocations is in the direction of $\langle 0\bar{1}11 \rangle$, and a few in the direction of $\langle 2\bar{1}11 \rangle$. The edges were calculated from the scalebar to be 1579nm. The area of the picture, calculated from the scale is then $2,49\mu\text{m}^2$ ($2,49 \cdot 10^6 \text{nm}^2$). Dislocation per area is measured in cm, which means $2,49 \cdot 10^{-8} \text{cm}^2$. This means that in this image, the dislocation density is $1,84 \cdot 10^9 \text{cm}^{-2}$.

Table 4-1 Density of dislocations from the area shown in Figure 4-5, Figure 4-7 and Figure 4-7

Area	$2,49 \cdot 10^{-8} \text{cm}^2$	Zone axis	$[\bar{1}\bar{2}1\bar{3}]$
Dislocation	46	Dislocation $\langle 0\bar{1}11 \rangle$	35
Dislocation density	$1,84 \cdot 10^9 \text{cm}^{-2}$	Dislocation $\langle 2\bar{1}11 \rangle$	9

4 Results

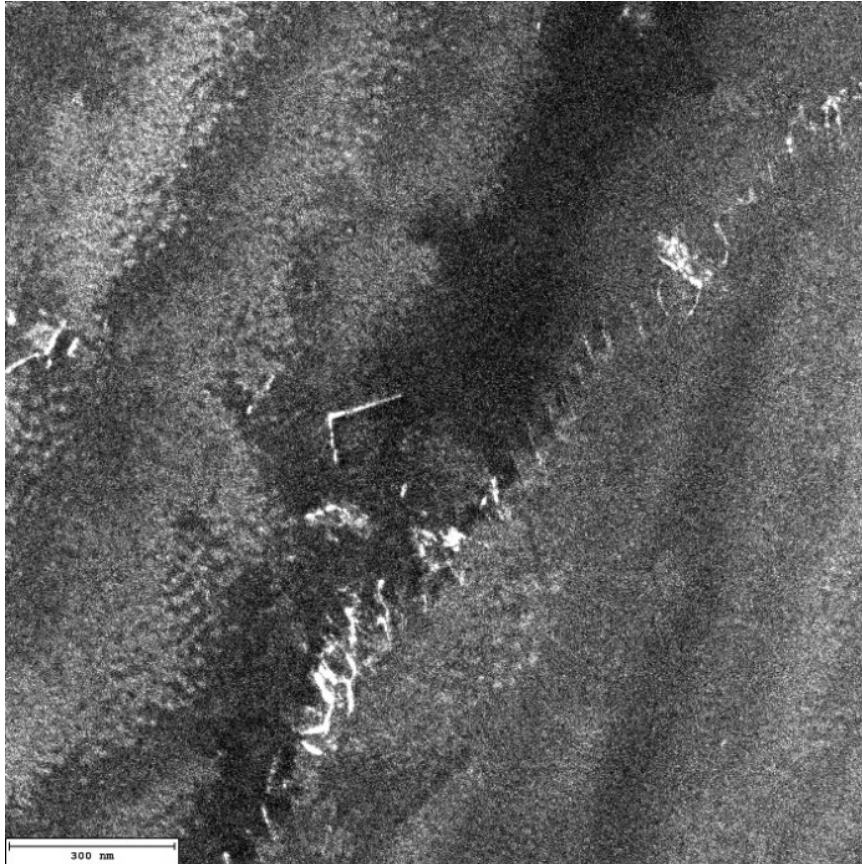


Figure 4-7 $[1\bar{2}1\bar{3}] \langle 0\bar{1}11 \rangle$ WB image taken from the area shown in Figure 4-5. The white lines shown here are dislocations. The area here are 1579^2nm^2 .

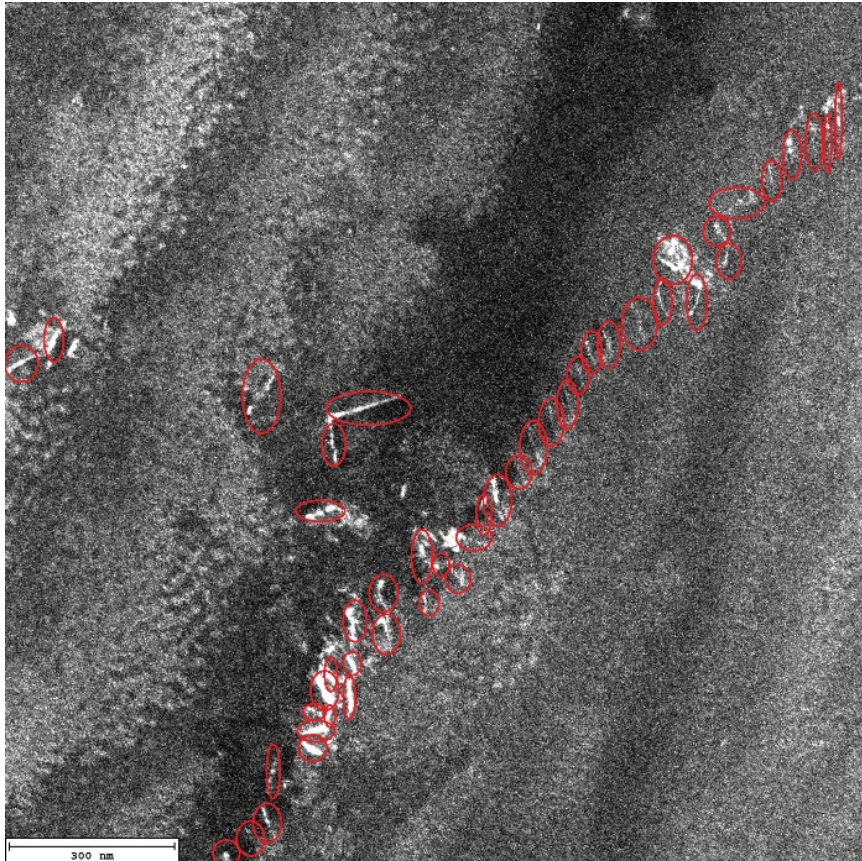


Figure 4-6 Same WB image as Figure 4-6 with the dislocations marked. The dislocations seem to follow a specific line which might mean that this is a slip plane.

4 Results

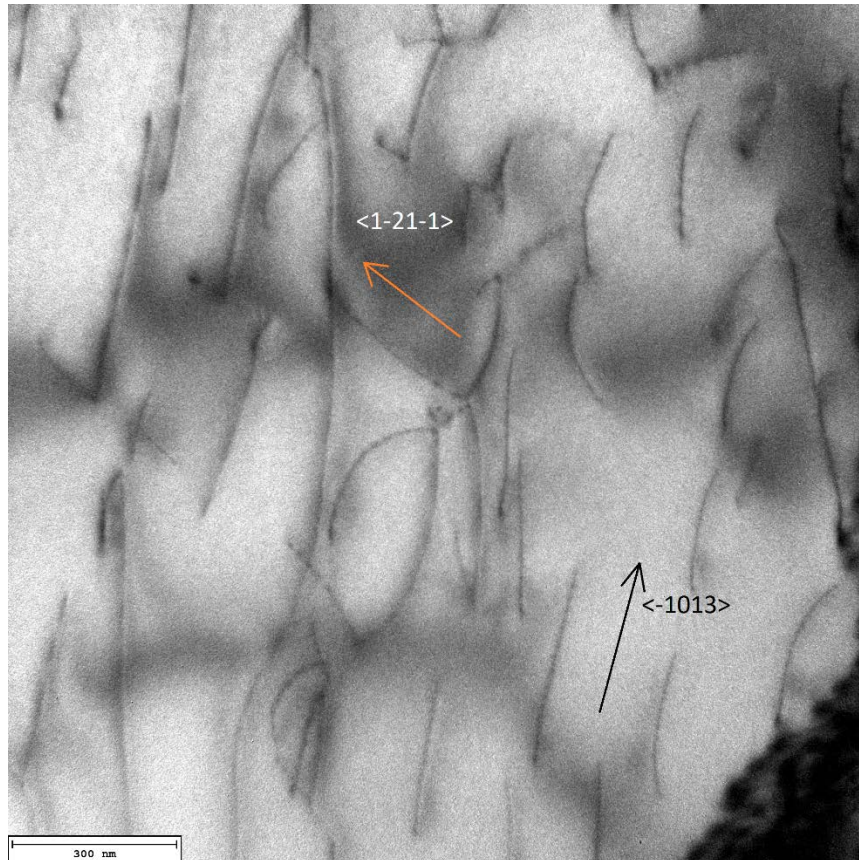


Figure 4-8 BF image of an area with dislocations. Zone axis of $[5\bar{1}43]$. The arrows show the directions. The dislocations seem to generally be one of the two.

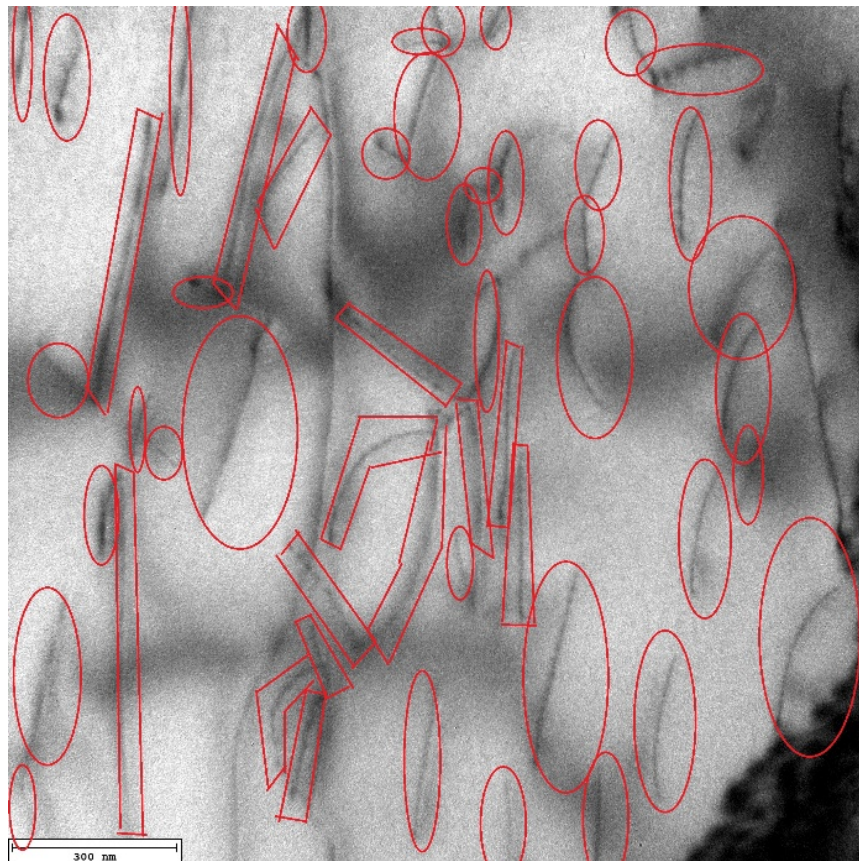


Figure 4-9 Same area as Figure 4-8, with marked dislocations. There are 53 dislocations. The area here is 1783^2nm^2 .

4 Results

In Figure 4-8 and Figure 4-9, shows an area of dislocations. These images have similar scalebar as the ones in Figure 4-7 and Figure 4-6. Calculation showed that edges was 1583nm compared to 1579nm from Figure 4-5. These two areas are treated as equal. Using the same area, the dislocation density can be calculated to $2,12 \cdot 10^9 \text{cm}^{-2}$. The directions of the dislocation seem to follow two directions. Most of the dislocations follow the direction of $\langle \bar{1}013 \rangle$, which is marked with a black line in Figure 4-8. A few of the dislocation lines follow a $\langle 2\bar{2}1\bar{1} \rangle$.

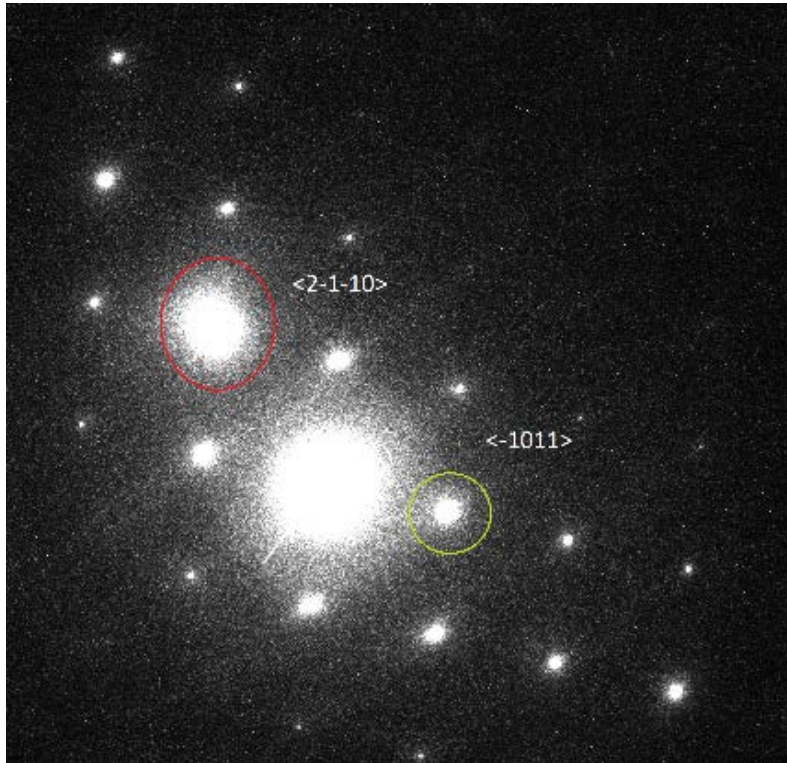


Figure 4-10 Diffraction image from zone axis $[01\bar{1}1]$ with reflections $\langle \bar{1}011 \rangle$ (green circle) and $\langle 2\bar{1}\bar{1}0 \rangle$ (red circle) marked. These two reflections are the basis for the weak beam image taken in

The types of dislocations are either edge dislocation, or screw dislocation, or a mix of both.

In order to find out a ratio of screw to edge, one of the perpendicular reflection to the burgers vector of the screw or edge. There are a few zone axis' that this is possible to do. The burgers vector for screw is $\langle 11\bar{2}0 \rangle$ and for the edge it is $\langle 0001 \rangle$. The diffraction image seen in Figure 4-10 has a zone axis of $[01\bar{1}1]$. In this zone axis, the reflection $\langle 2\bar{1}\bar{1}0 \rangle$ is present. Choosing this reflection means to cancel out the burgers vector for the edge dislocation, and effectively hiding them. In the Figure 4-12, the reflection is $\langle \bar{1}011 \rangle$. This means that all the dislocations are visible. The number of dislocations here are 45, and the area is $1,40954 \cdot 10^{-8} \text{cm}^2$. This gives a density of $3,19 \cdot 10^9 \text{cm}^{-2}$. A little higher than the other regions. Comparing this to the image taken with the reflection $\langle 2\bar{1}\bar{1}0 \rangle$ would give a ratio of edge to

4 Results

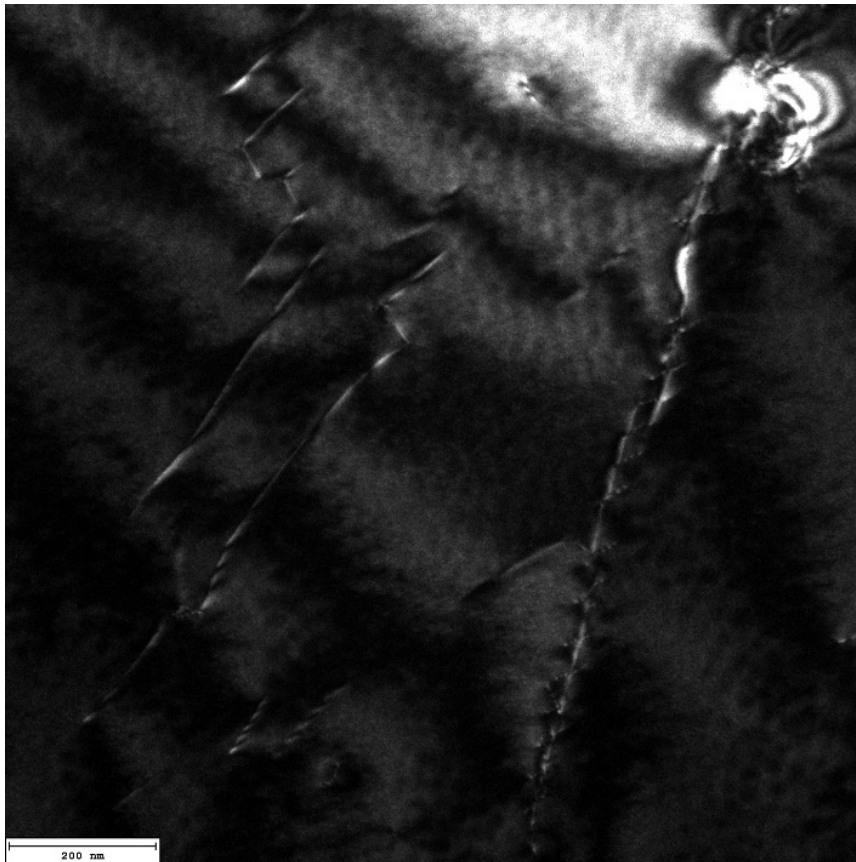


Figure 4-12 Weak beam image taken from the reflection $\langle\bar{1}011\rangle$ from the diffraction image seen in Figure 4-10. Area is calculated to be $1,40954 \cdot 10^{-8} \text{cm}^2$.

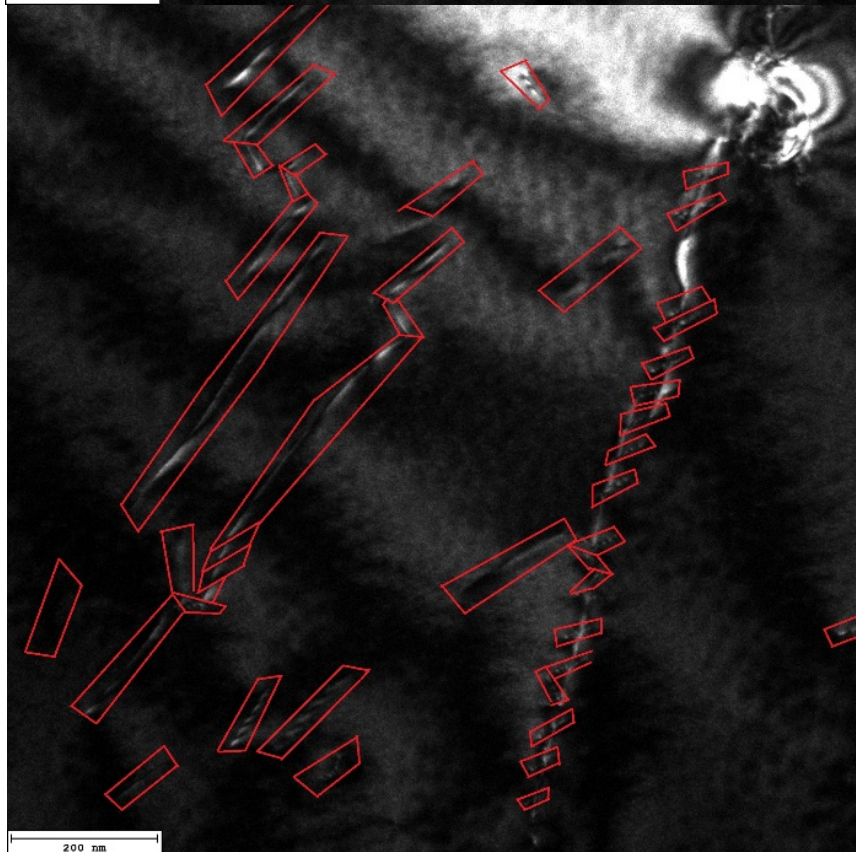


Figure 4-11 Same Weak beam image from Figure 4-12 with marked dislocations. 45 dislocations are present here

4 Results

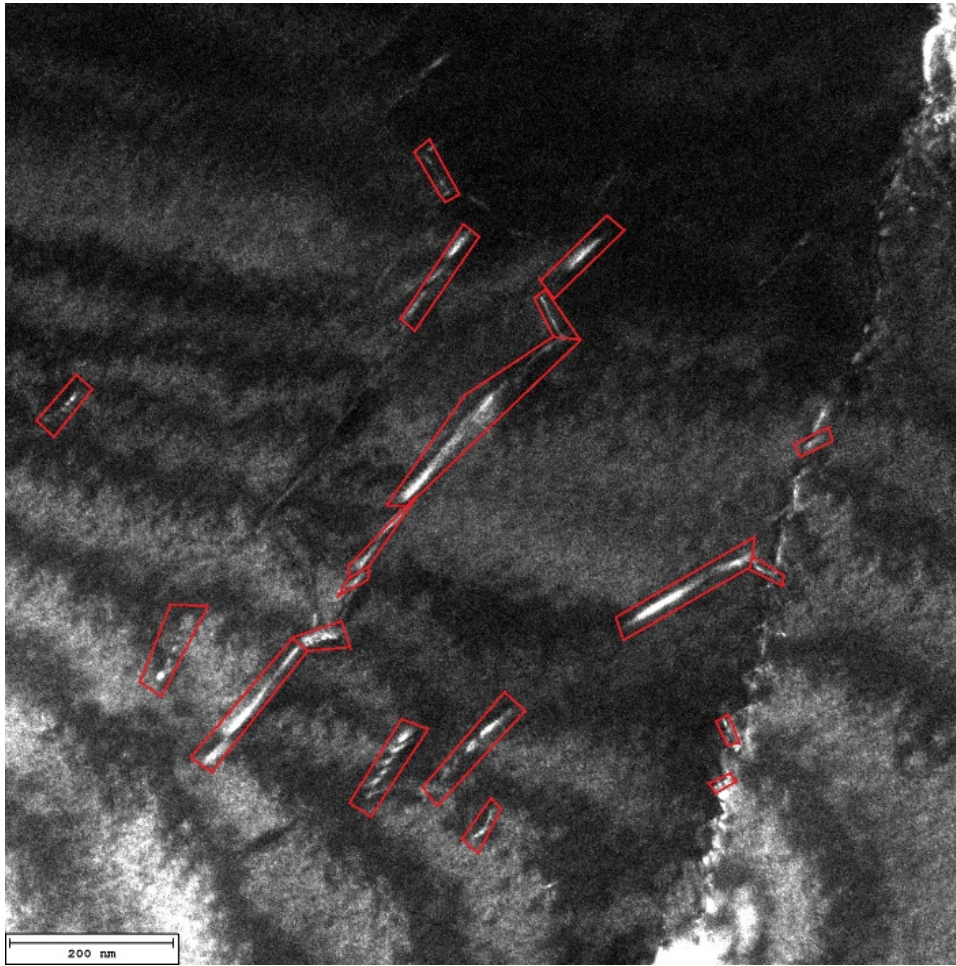


Figure 4-13 Weak beam image taken from $\langle 2\bar{1}\bar{1}0 \rangle$. The criterion $\vec{g} \cdot \vec{b} = 0$ is fulfilled for edge dislocations here. The remaining dislocation are marked. The 19 remaining dislocations can only be screw or mixed type.

screw and mixed. In the image from Figure 4-13 all of the edge dislocations are gone. The only dislocations that are visible here, are the screw dislocation, and those that are a mix of both screw and edge. When counting the dislocations present, there was 19, meaning that 26 are gone. The density of dislocations here is $1,35 * 10^9 cm^{-2}$. This density is the amount of pure edge dislocations, meaning that there are 42,22% pure edge dislocations, and 57,58% of screw and mixed. The general direction of the dislocations in this area is $\langle 0\bar{1}12 \rangle$

Using the Taylors equation $\tau = \alpha \mu b \rho^{\frac{1}{2}}$ and the flow stress equation $\sigma = \sigma_0 + k \rho^{\frac{1}{2}}$ we can find the flow stress in these areas. $\sigma = \sigma_0 + \alpha \mu b \rho^{\frac{1}{2}}$. Values taken from Table 2-4 Collected from (Abbaschian & Reed-Hill, 2011) and (P.Rodriguez-Calvillo & J.M.Cabrera, 2015) are used to calculate. In the Table 4-2 the various flow stresses are calculated. The average flow stress is 298MPa in these areas.

4 Results

Table 4-2 Flow stress calculations, dislocation densities are in m

Zone axis/figure	Dislocation density, ρ	Flow stress, σ
$[\bar{1}\bar{2}\bar{1}\bar{3}]$ / Figure 4-7	$1,84E+9 \text{ cm}^{-2}$	296MPa
$[5\bar{1}\bar{4}3]$ / Figure 4-8	$2,12E+9 \text{ cm}^{-2}$	297MPa
$[01\bar{1}1]$ / Figure 4-12	$3,19E+9 \text{ cm}^{-2}$	301MPa

The strain energy for screw can be calculated to $W_e = \frac{\mu b^2}{4\pi} * \ln \frac{4r'}{b}$. The strain energy of edge dislocations can be calculated to $W_e = \frac{\mu b^2}{4\pi(1-\nu)} * \ln \frac{4r'}{b}$. This means that the strain energy for edge dislocations are higher than screw with a factor of $1/(1 - \nu)$. The poisson's ratio for titanium is 0.3. Which means that edge dislocations have about 50% more strain energy. (Abbaschian & Reed-Hill, 2011)

4 Results

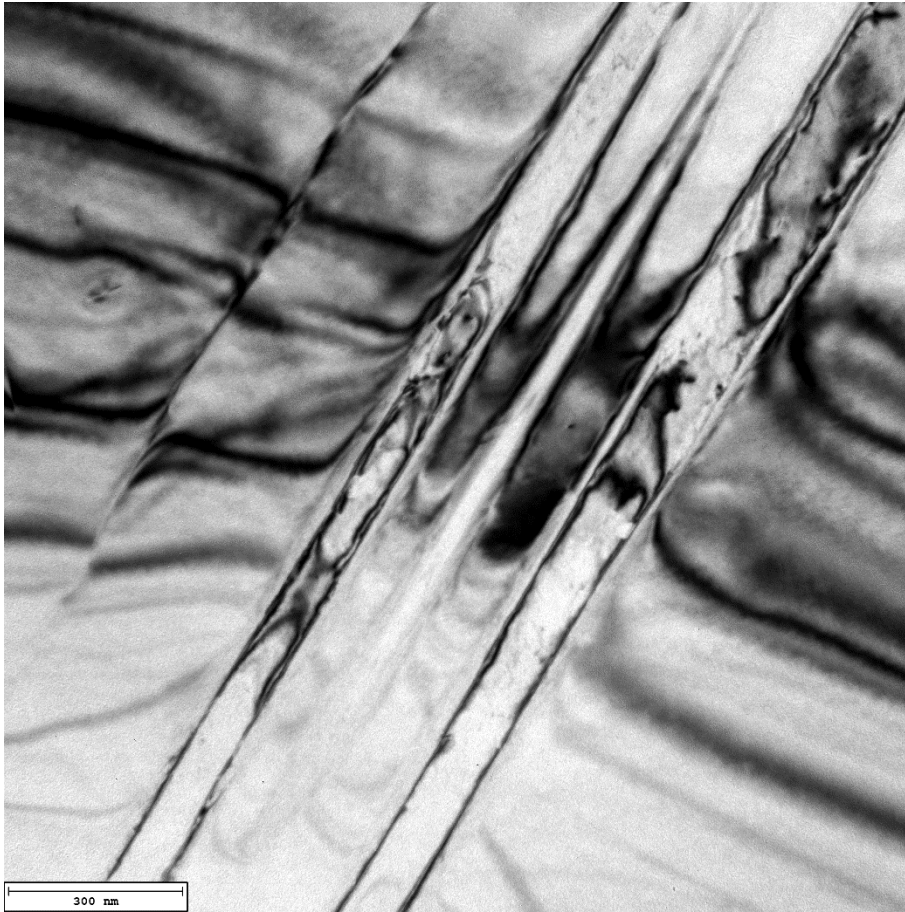


Figure 4-14 Deformed twinning structure with retained β phase.

Studying the microstructure of the Ti, there were also found structures similar to the one in Figure 4-14. Long structures with diffuse edges. The diffraction pattern can be seen in Figure 4-17 and shows two underlying systems. The majority of spots is the diffraction pattern of hcp α -phase with the zone axis of $[5\bar{1}43]$. The spots that do not correspond to the same zone axis can be seen as only a few spots in the diffraction image. Weak beam images was taken of the marked reflections in Figure 4-17. Measurement of the d-space between the center beam and the closest of these spots (green circle in Figure 4-17) was measured to be 5,0317 1/nm. This corresponds to 1,987Å. Comparing this to other known distances shows that it matches the bcc β -phase of titanium of $d_{111}=1.917\text{Å}$.

4 Results

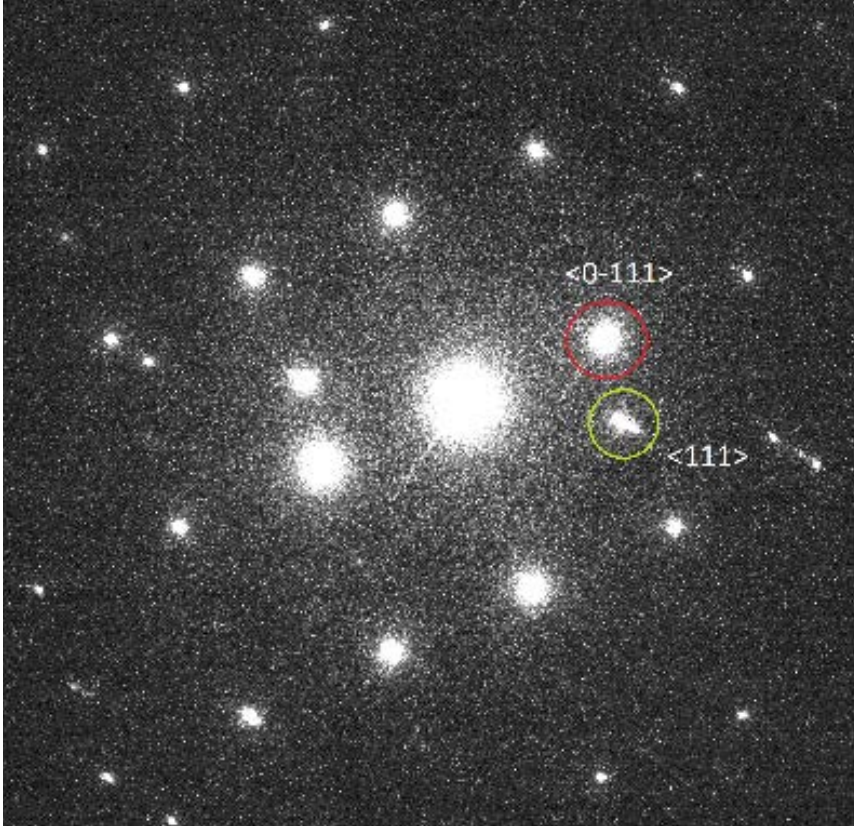


Figure 4-17 Diffraction image with majority of spots corresponding to the hcp crystal with zone axis of $[5\bar{1}43]$. The reflections that are marked, belong to bcc b_{111} .

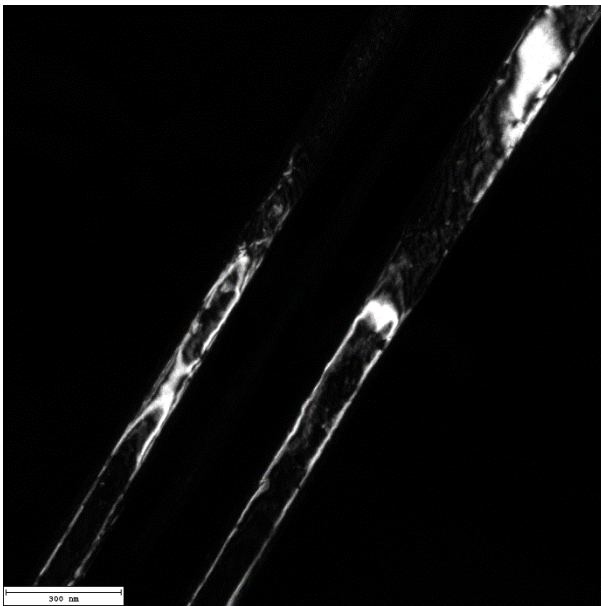


Figure 4-16 Weak beam image formed from the reflection shown in green circle Figure 4-16. This shows that the inside of this this elongated structure is from the system that is from the reflection chosen of $\langle 111 \rangle$

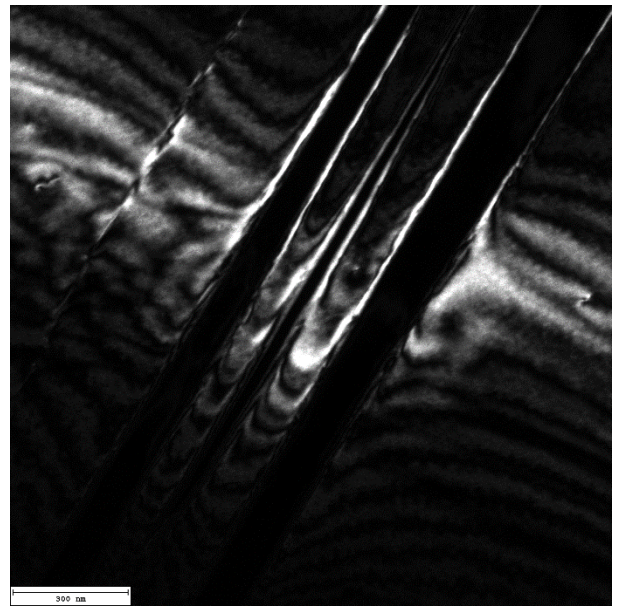


Figure 4-15 Weak beam image of the reflection in the red circle showing that the outside of the elongated structure belongs to hcp with zone axis $[5\bar{1}43]$

4 Results

4.4 EBSD of thick sample in XY plane

In the EBSD, from the thick sample. There are taken samples from the plane XY. The samples are taken from the inside, towards the non-machined surface where x is smallest (Figure 3-1). The middle, and the outside, towards the machined surface. The inside non-machined surface is also exposed to the argon environment during the manufacturing process.

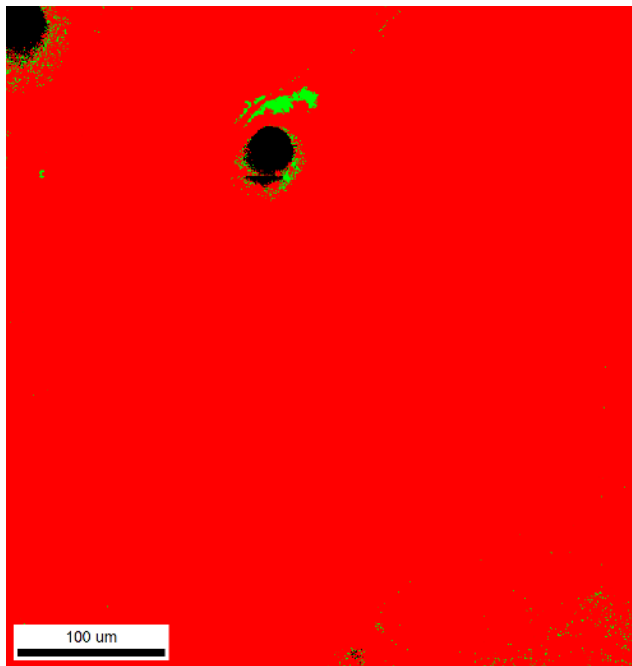


Figure 4-18 Taken from the sample closest to the inside. Where surface is non-machined. The phases are marked with α -phase (red) and β -phase (green). Of the sample taken. This was the only sample with any measurable amount of β -phase. The EBSD showed that it is 98.5% α , and only 0.6% β -phase

Titanium (Alpha); 0.985; 0.985;

Titanium (Beta); 0.006; 0.006;

The three samples can be seen in Figure 4-18 and Figure 4-20. The β -phase is marked with green. This β phase is only detectable in the sample which is taken near the area of the surface which is not machined. This is the image seen in Figure 4-18. The surface of the non-machined side, the inside. This surface is also the only part of this component that was exposed to the argon atmosphere during the manufacturing. Seeing as the presence of β -stabilizers in this materials is nonexistent. The only reason for the retained β -phase here is increased cooling rate, as shown in the cooling rate study (Chun & Wenfeng, 2010). Seeing as there is only β -phase of any noticeable amount near this surface could mean that the heat dissipates more quickly to the argon gas than in the titanium itself.

4 Results

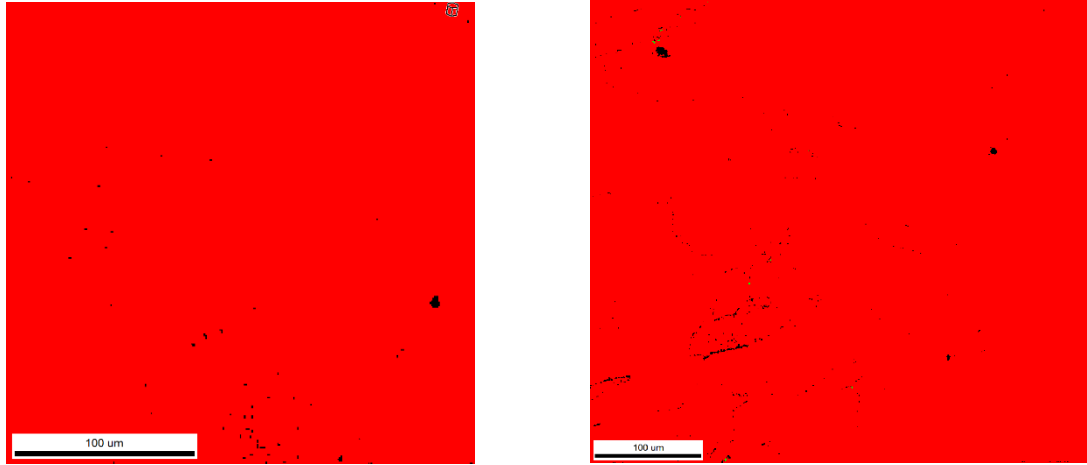


Figure 4-20 The sample taken from the middle of the area (left) shows no β phase. Neither does the sample close to the outside, where the machined surface lies. The phases is marked by red, α -phase. β -phase is marked green, but none is present.

Studying the misorientation angles (Figure 4-19) of the different samples reveals peaks at angles at 65° and 86° . According to a study (Xu, et al., 2017) the 86.3° angle (tolerance of $\pm 5^\circ$) correspond to $\{10\bar{1}2\}\langle 10\bar{1}1\rangle$ tensile twin. The angle of 65° corresponds to the $\{10\bar{1}2\}\langle 10\bar{1}1\rangle$ compressive twinning. There is peak at 34° which can match the tensile twinning of $\{11\bar{2}1\}\langle \bar{1}\bar{1}26\rangle$.

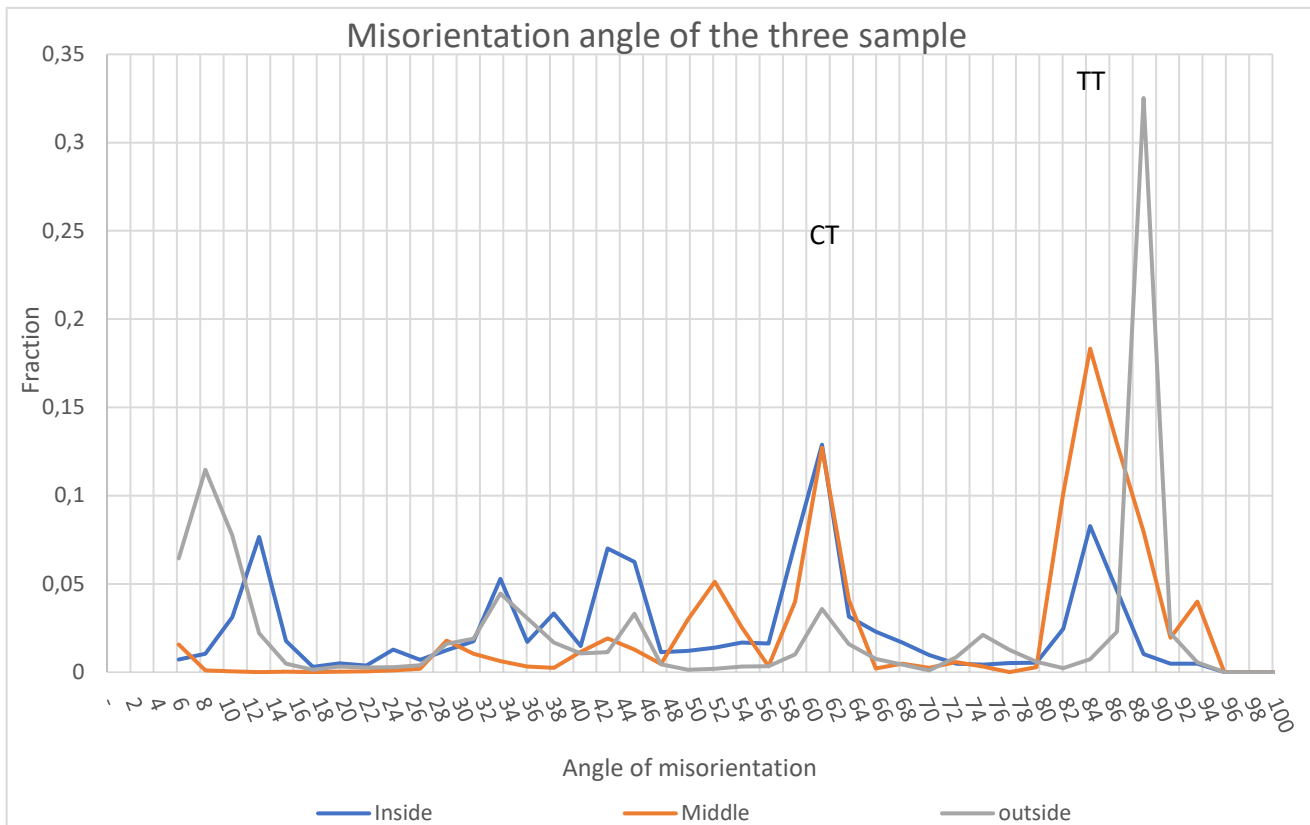


Figure 4-19 The misorientation angles of the three samples. There are clear peaks located around 60° and 90° . According to (Xu, et al., 2017) these are compression twin (CT) and tension twin (TW). These are marked.

4 Results

Looking at the samples and pointing out these boundaries will give more information on the twinning. First sample is the one on the inside, near the non-machined surface. In Figure 4-21 the boundaries are

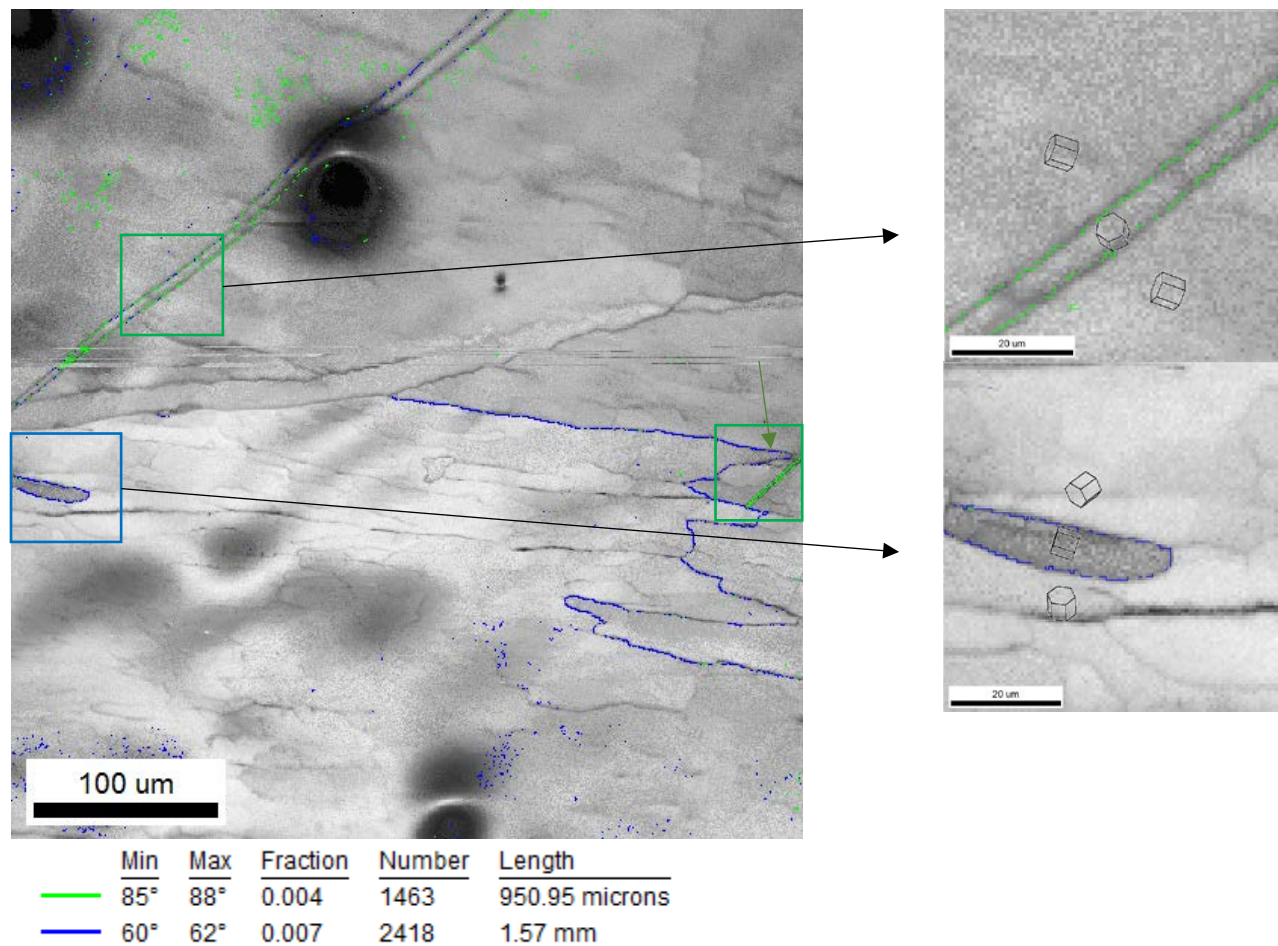
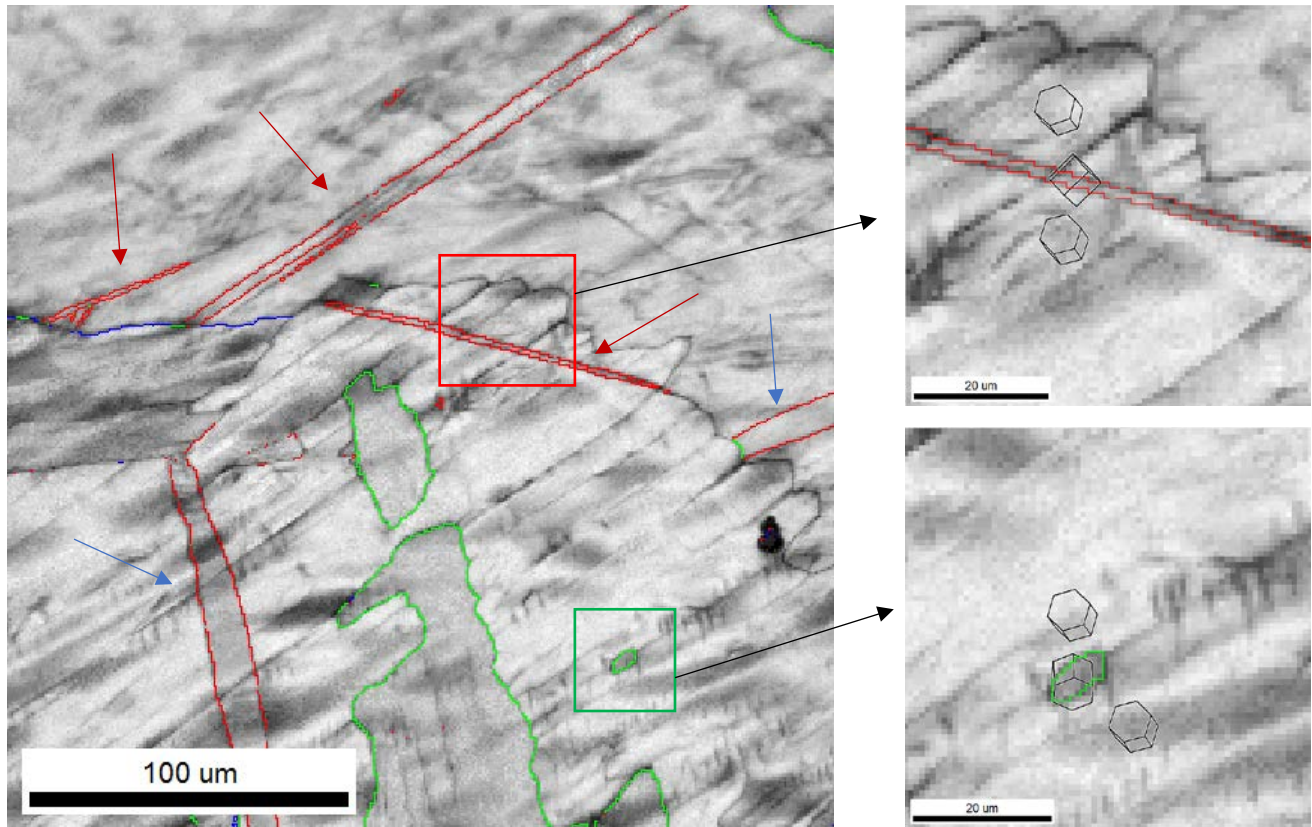


Figure 4-21 Sample taken from the inside sample. The misrotation angle that matches the peaks is shown. Both tensile twin area marked green and compressive twin area marked blue. To the right, a zoomed in view of the twins can be seen along with the crystal orientation. The needle like structures are tensile twins marked with green borders. The compressive twins should have been seen here in blue border. A zoomed in picture of a grain (blue border) with misrotation matching the compression twin can be seen to the right. A small twin can be seen to left in image with green box and green arrow.

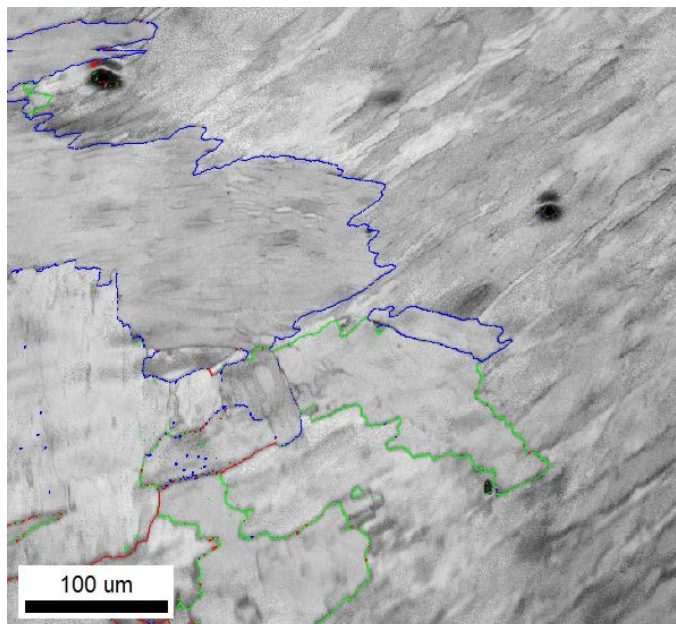
outlined in the inside sample according to the peaks in Figure 4-19. Both twinning deformation systems are present here. Showing the blue boundary matches $\{10\bar{1}2\}\langle 10\bar{1}1\rangle$ compressive twinning and the green boundary matches $\{10\bar{1}2\}\langle 10\bar{1}1\rangle$ tensile twin. The next sample to study is the middle sample. In the middle sample there are a few peaks. The interesting ones are the peaks in the 65° and 86° area. In the Figure 4-23 the twinning structures are more prominent and easier to spot. Marked with red arrows these needle type structure are easy to spot. The two structures with blue arrows does not have the typical needle like structure of the tensile twins so they are disregarded. The last sample is the one taken near the outside. Closer to the machined surface. When checking the outside sample for

4 Results



	Min	Max	Fraction	Number	Length
—	82°	88°	0.042	1676	1.34 mm
—	57°	65°	0.022	887	709.60 microns
—	40°	47°	0.005	178	142.40 microns

Figure 4-23 Sample taken of the middle area. Tensile twins are marked with red arrows $\{10\bar{1}2\}\langle 10\bar{1}1\rangle$. The misrotation angle boundaries that matches the compression twin of $\{10\bar{1}2\}\langle 10\bar{1}1\rangle$ is marked in green. But there is no obvious compression twin structure.



	Min	Max	Fraction	Number	Length
—	30°	40°	0.009	1420	923.00 microns
—	5°	15°	0.016	2527	1.64 mm
—	85°	90°	0.019	3051	1.98 mm

Figure 4-22 Sample taken from the sample closest to the outside surface. The misorientation peaks seen in Figure 4-19 is marked and color coded. There are no twinning structure. The area that matched the 35° $\{11\bar{2}1\}\langle \bar{1}\bar{1}26\rangle$ twin, does also not show any twinning deformities.

misorientation boundaries it becomes apparent that there are no twin structure in this sample. After reviewing the samples the area in the middle of the thick sample is the area with most twinning

4 Results

deformities. The twinning deformities are not present in the outside sample, towards the machined surface. Through the sample the misorientation seems to focus towards 60-65° and 85-90°. The reason for this is two folds. One is the location of tensile twins and compressive twins which could reside in there angle areas. The other reason is that the misorientations between the $\langle 110 \rangle_{\beta}$ plane form at either 90° or 60°. It is also shown in a study (Bieler & Semiatin, 2001) that when Ti is reheated to β phase, and subsequently cooled down the reverse transformation will form in an orientation that is different to about 90° or 60°. The higher peak in the outside sample around 90° shows a preferred orientation difference. This 90° rotation could be explained by a mutual alignments of the β boundary. Taking in to effect the size of the grain it is not possible to definitely prove.

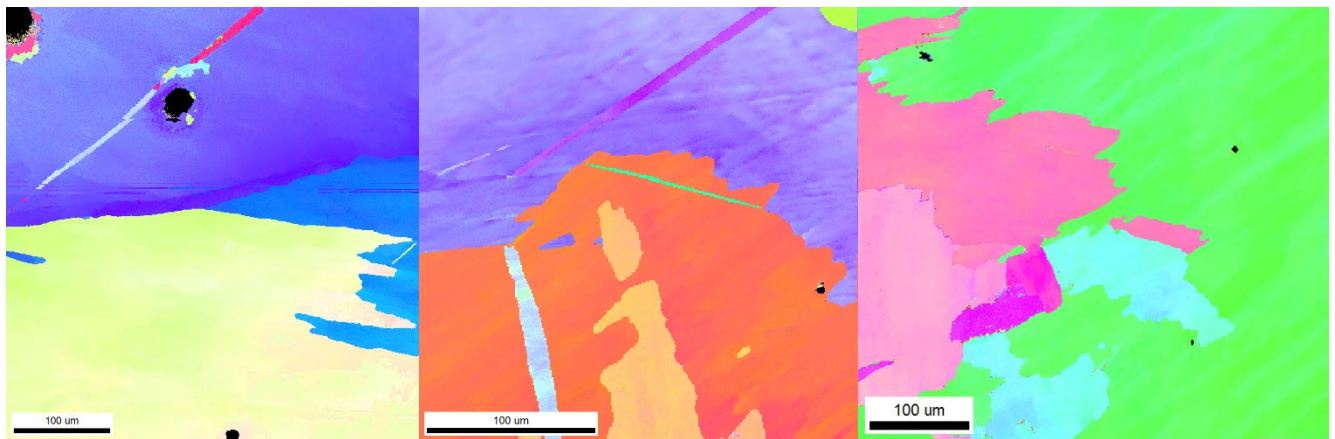


Figure 4-24 The inside sample (left), the middle, and outside sample (right). Comparing the samples there is an increasing in the subgrains. The inside has large grains, while the outside sample has smaller subgrains down to $\sim 50\mu\text{m}$

Comparing the grains of the samples. The inside sample has grains that are too large to measure in this sample. The middle sample has a few subgrains. In the outside sample, the subgrains are more numerous.

4 Results

4.5 EBSD of thin sample in both XY and YZ plane

The samples of thin sample are taken to compare difference in the two planes. Samples here are simply referred to as XY and YZ. The orientation of the two planes can be seen in Figure 4-27. The XY plane has boundaries mostly focused in the angle of 55°-65°. A peak in the XY sample matching a twinning

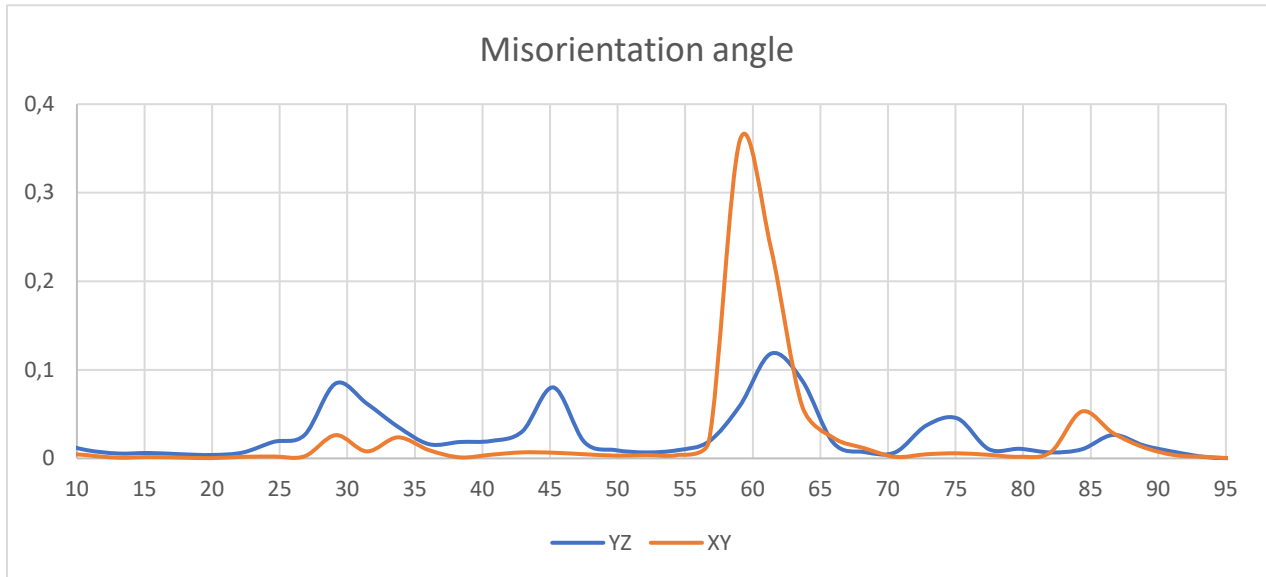


Figure 4-27 Misorientation angle chart of XY and YZ plane

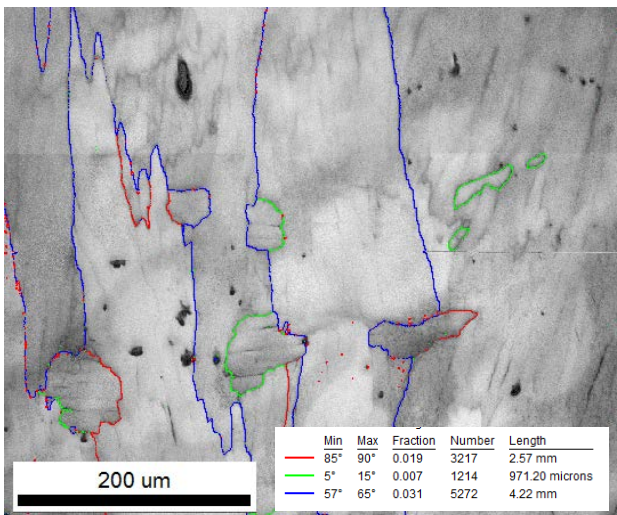


Figure 4-26 Sample YZ from YZ plane. The marked boundaries are the most prominent ones.

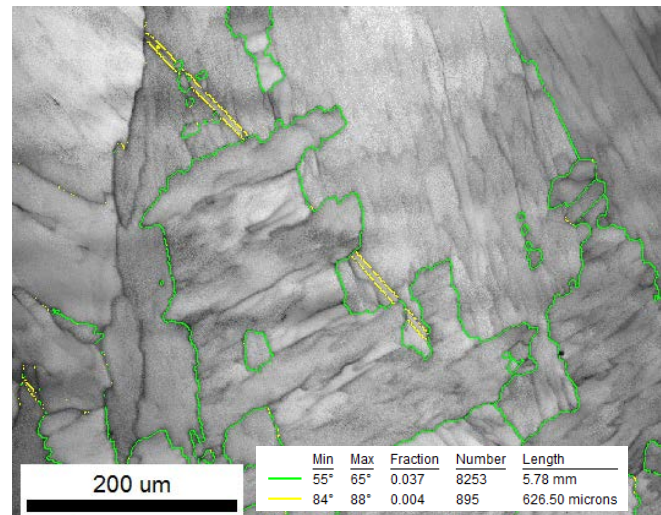


Figure 4-25 Sample XY from XY plane. Twinning deformity marked in yellow.

deformity can be seen in chart at 85°. This twin can also be seen in the XY sample, marked in yellow in the Figure 4-25. The high peak at 60° coincide with the misorientation of $\langle 001 \rangle_{\beta}$ plane on which α can form precipitates when cooling are either 60° or 90°. With 60° boundary orientation having twice the occurrence in arbitrary variant selection. When looking at the $\{110\}_{\beta}$ plane, four give rise to 60

4 Results

The size of the grains are larger in the YZ plane. Studying in the YZ plane, samples needed to be large enough. In Figure 4-28 the first sample from the YZ plane was taken. One grain almost cover the entire sample size. The grains in the YZ plane have more elongated plate α -phase. This is probably because the



Figure 4-28 A sample from the YZ plane. A grain almost take up the whole sample size.

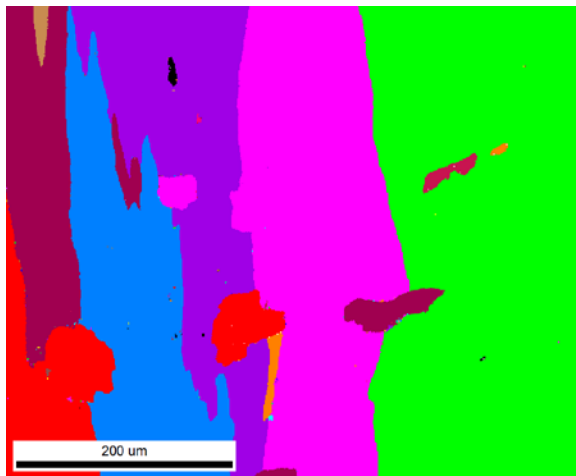


Figure 4-30 The sample from the ZY plane with grains marked. The elongated columnar grains are really visible here. 13

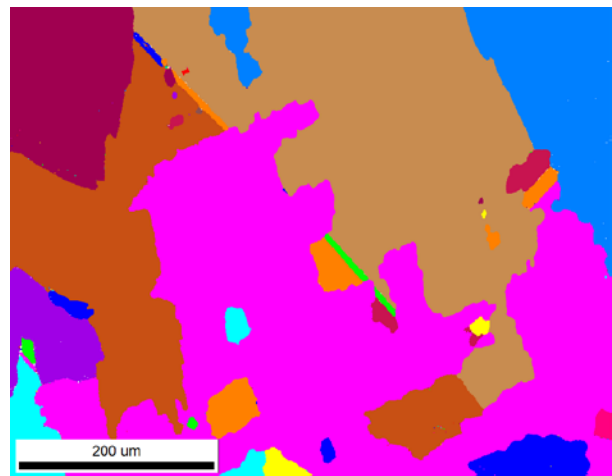


Figure 4-29 The sample from the XY. Small subgrains here varying from 10-80 micrometer. Although no elongation. The grains have comparable size to the YZ plane, but there are more subgrains here.

epitaxial growth is closer to this direction than the XY plane. Which follows the literature study of solidification of the columnar grains. The size of the grains cannot be differentiated because some go outside the sample area. There are more subgrains in the XY plane. The subgrains vary in size going 5-80 μ m in size in the XY plane. Looking at the pictures in Figure 4-31, it is shown the crystal orientation. With this it is possible to that some small grains were once probably from the same grain.

4 Results

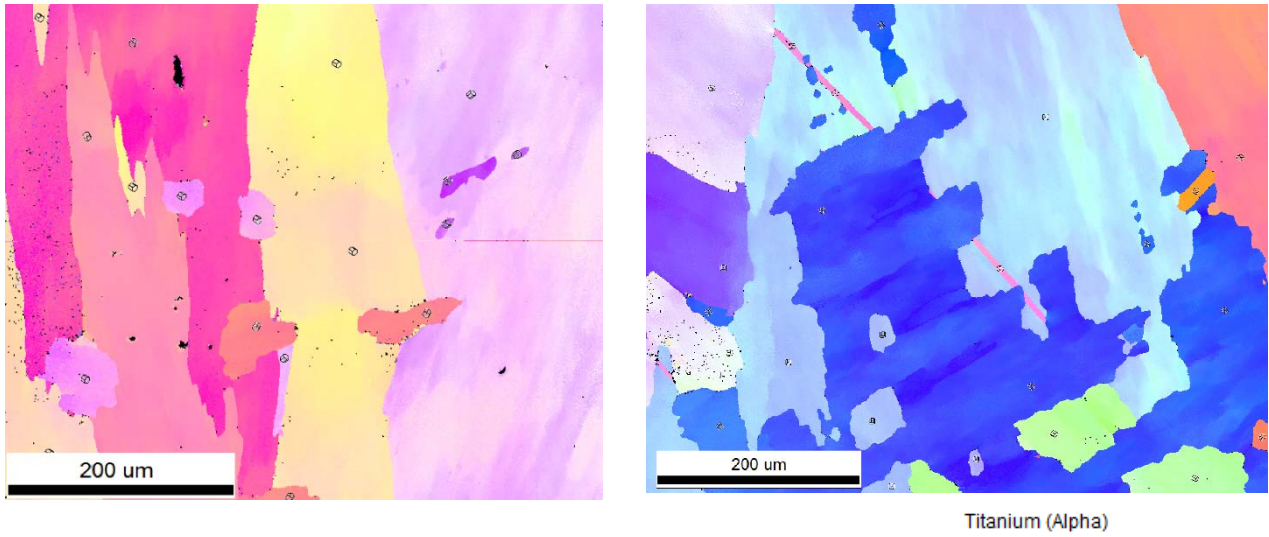
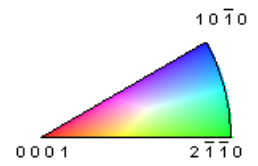


Figure 4-31 The Sample from XY plane (right) and the YZ plane (left) show that many of the subgrains were once a part of the same grain.



5 Discussion and conclusion

5 Discussion and conclusion

In the TEM study it was found areas of dislocations. The dislocations were counted and its density was measured. The densities found were $1,84 \cdot 10^9 \text{cm}^{-2}$, $2,12 \cdot 10^9 \text{cm}^{-2}$ and $3,19 \cdot 10^9 \text{cm}^{-2}$. These were all in the order of 10^9cm^{-2} . The calculated flow stress because of the dislocations densities were calculated to be averaging 298MPa. The direction of the dislocations can be seen and generally takes one or two directions, where one is more prevailing. The density of screw+mixed dislocation was found to be $1,35 \cdot 10^9 \text{cm}^{-2}$ in the area with $3,19 \cdot 10^9 \text{cm}^{-2}$. Meaning that the pure edge dislocation can be calculated to be $1,84 \cdot 10^9 \text{cm}^{-2}$. Concluding that the samples area contain more edge dislocations, compared to screw. The strain energy of screw and edge have a $1/(1-\nu)$ difference. With the poisson ratio to Ti being 0.3. This leads to a 50% higher strain energy for edge dislocations. The same can be said for the stress field which is also higher for edge dislocation by $1/(1-\nu)$. This leads to a increased stress for the Ti. For cp-Ti grade 2, the poisson ratio could be as higher leading to even higher strain. In 1961 Venables (Venables, 1961) managed to correlate dislocation climbing, or more specifically the movement of edge dislocation to another slip plane called jogging. Could be considered as twin nucleus in fcc materials. This might carry over to hcp and act as twin nucleation during deformation. The increased edge dislocation could also form basis for twin nucleation. Increased jogging could also contribute to work hardening of the material because of the 'frictional' drag (Smallman & Ngan, 2014, p. 128). Elongated twin-like structures was observed containing β -phase with $\langle 111 \rangle$. The $\langle 111 \rangle$ could correspond to $\{112\}\langle 111 \rangle$ slip system of β .

In the study of the thick sample made of two wires. There was identified β -phase near the surface which is exposed to the argon gas. Seeing as there are no β -stabilizers this area must have had a high enough cooling rate of above 15°C/s to form retained β -phase. The misorientation angles showed peaks at 60° and $85\text{-}90^\circ$. Tensile twins were found in the sample taken near the inside surface, and the middle ones. Corresponding to the 85° . Twinning were most prevailing in the middle sample. I can speculate that this is the area conjunction of the two wires. No compression twins were found that could correspond to 65° . Twinning were found most prominent in the middle sample. The peaks at 60° and 90° can correspond to angles that are formed in the transformation phase $\alpha \rightarrow \beta$ and $\beta \rightarrow \alpha$. When α forms on the $\{001\}\beta$ which can have angle of 90° or 60° . In the sample closest to the machined surface there were more prevailing 90° . Because of the size of the grain it is not possible to definitely prove a correlation. But it could be boundary between the large grains have a mutual alignment. It could also mean that the transformation of β causes a bias on the variant with the angle of 90° .

5 Discussion and conclusion

The thin sample made of one wire has shown the elongated grains in the YZ plane. This corresponds to the epitaxial growth of the columnar β grains, see Figure 2-4. Both planes studied of the thin sample showed a misorientation peak of 60° . There is the presence of tensile twinning deformation in the XY plane which corresponds to a 85° . The peaks at 60° corresponds to the increased misorientation occurrence compared to the 90° (Bielera & Semiatin, 2001).

The reason for the tensile twinning could be because of the transformation and the atomic density of the hcp crystal and the bcc crystal. The density of hcp is 6 atoms in 0.106nm^3 resulting in $56,6\text{nm}^{-3}$. For bcc there are 2 atoms in 0.0366nm^3 leading to $54,6\text{nm}^{-3}$. This means that during the transformation from hcp to bcc, the atomic density goes up and causes a tensile stretch. This might be the cause for tensile twinning deformities in the sample. From the middle sample taken of the thick specimen made with two wires, there are more tensile twins. This could be because this is in the area of conjunction of the two wires.

6 References

6 References

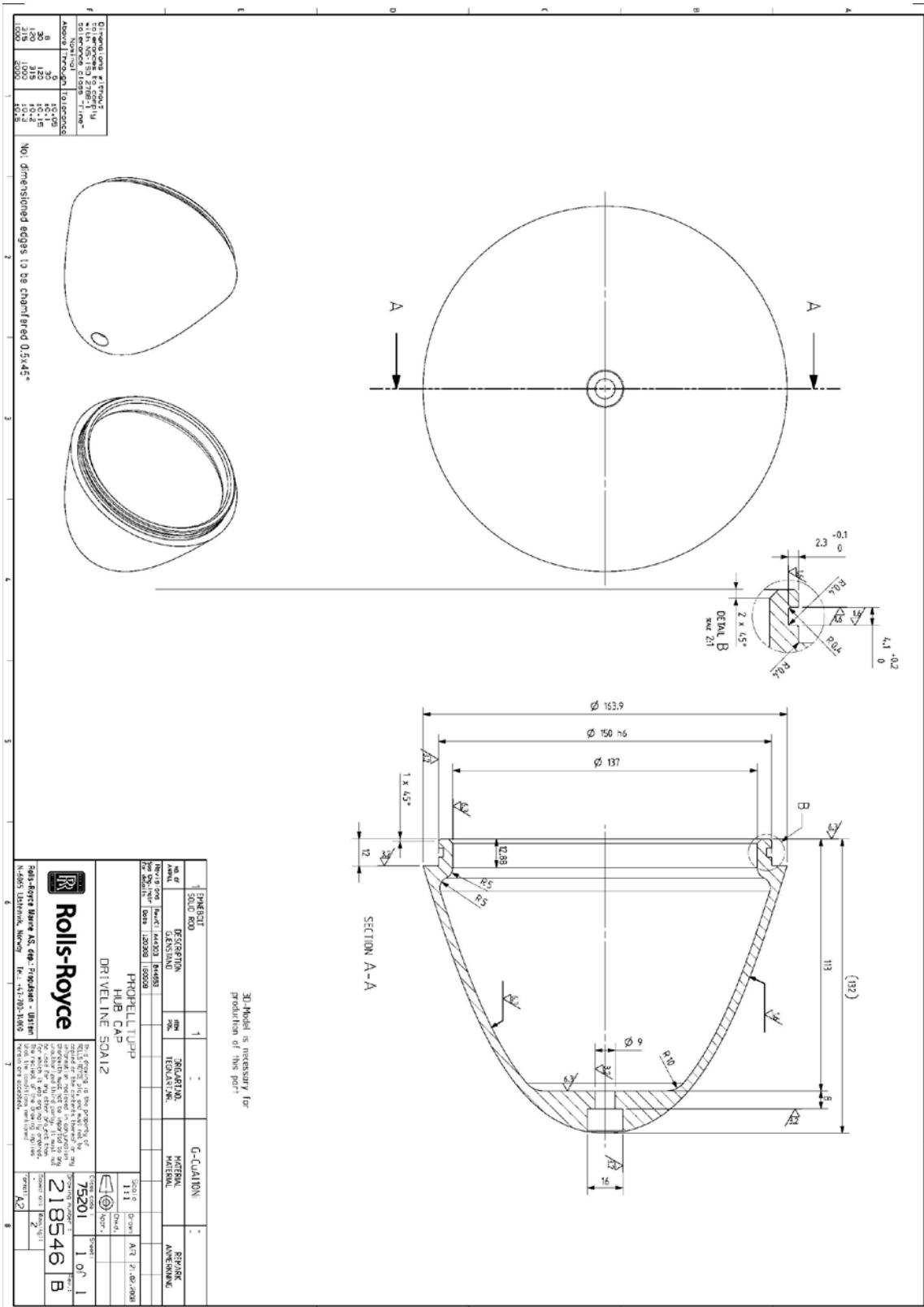
- Abbaschian, R. & Reed-Hill, R. E., 2011. *Physical Metallurgy Principles*. 4th ed. s.l.:CL-engineering.
- ASM International, n.d. *Metals handbook Volume 3 - Alloy phase diagram*, s.l.: s.n.
- Banerjee, D. & Williams, J., n.d. Perspectives on titanium science and technology *Acta Mater.* 61 (2013) 844-879..
- Bielera, T. R. & Semiatin, S., 2001. The origins of heterogeneous deformation during primary hot working of Ti-6Al-4V. *International journal of plasticity*, pp. 1162-1189.
- Bill Taylor (Struers Ltd, G. & Elisabeth Weidmann(Struers ApS, C., 2015. *Application Note: Metallographic preparation of titanium*, s.l.: s.n.
- Burgers, W., 1934. *On the process of transistion of the cubic-body-centered modification into the hexagonal-close-packed modification of zirconium*, s.l.: s.n.
- Christian, J. W. & Mahajant, S., 1995. DEFORMATION TWINNING. *Progress in Material science*, Volume 39, pp. 1-157.
- Chun, X. & Wen-feng, Z., 2010. Transformation mechanism and mechanical properties of commercially pure titanium. *Elsevier*.
- Delimitis, A., 2018. *Thesis meeting and discussion [Interview]* (April 2018).
- Dieter, G. E., 1986. *Mechanical Metallurgy*. London: McGraw-Hill Book company.
- Edington, J. W., 1975. *Electron diffraction in the electron microscope*. 1st ed. London and Basingstoke: The macmillan press .
- ELMER, J. W., WONG, J. & RESSLER, T., n.d. Spatially Resolved X-Ray Diffraction Phase Mapping and alpha to beta to alpha Transformation Kinetics in the Heat-Affected Zone of Commercially Pure Titanium Arc Welds.
- Grong, Ø., 1997. *Metalurgical modelling of welding*. s.l.:s.n.
- KEHAGIAS, T. et al., 1994. INTERFACIAL DISLOCATION ARRAYS IN TWIN BOUNDARIES OF DEFORMED TITANIUM. *pergamon*, November.
- Lai, M., Tasan, C. & Raabe, D., 2016. On the mechanism of {332} twinning in metastable b titanium alloys. 12 March.
- Laine, S. J. & Knowles, K. M., n.d. {11⁻24} deformation twinning in commercial purity titanium at room temperature.
- Leyens, C. & Peters., M., n.d. *Titanium and titanium alloys: fundamentals and applications*. s.l.:s.n.
- Lutjering, G. & Williams, J. C., 2007. *Titanium, 2nd Edition (Engineering Materials and Processes)*. 2nd edition ed. s.l.:s.n.
- Meyers, M. & Chawla, K., 2009. *Mechanical Behavior of materials*. 2nd ed. s.l.:Cambridge University Press.

6 References

- Mukhopadhyay, S. B. a. P., 2007. *Phase Transformations_ Examples from Titanium and Zirconium Alloys*. s.l.:s.n.
- Nervo, L. et al., 2015. A study of deformation twinning in a titanium alloy by X-ray diffraction contrast tomography. *Acta Materialia*, Volume 105.
- Norsk Titanium, 2010. *NTiC Technical Presentation*, s.l.: s.n.
- P.Rodriguez-Calvillo & J.M.Cabrera, 2015. Microstructure and mechanical properties of a commercially pure Ti processed by warm equal channel angular pressing. *Material science and Engineering*, Volume 625, pp. 311-320.
- PADILLA, H. et al., 2007. Effects of Deformation Twinning on Energy Dissipation in High Rate Deformed Zirconium. *ASM international*.
- Shindo, D. & Oikawa, T., 2002. *Analytical Electron Microscopy for Materials Science*. 1st ed. s.l.:Springer Tokyo.
- Sinha, S. et al., 2017. Effect of initial orientation on twinning in. *Philosophical Magazine*, 17 January.
- Smallman, R. E. & Ngan, A. H. W., 2014. *Modern Physical*. 8th ed. s.l.:Elsevier Ltd.
- Stempfer, F., 2011. *Method and arrangement for building metallic objects by solid freeform fabrication*. US patent, Patent No. US20170001253A1.
- Tirrya, W. et al., n.d. Twinning in pure Ti subjected to monotonic simple shear deformation.
- Venables, J., 1961. Deformation twinning in face-centred cubic metals. *The Philosophical Magazine: A Journal of Theoretical Experimental and Applied Physics*, 6(63), pp. 379-396.
- Vera, M. L. et al., 2017. Evaluation of the influence of texture and microstructure of titanium. *Materials Characterization 131 (2017) 348–358*.
- Williams, D. B. & Carter, C. B., 2009. *Transmission Electron Microscopy*. 2nd ed. s.l.:Springer.
- WILLIAMS, J., BAGGERLY, R. & PATON, N., 2002. Deformation Behavior of HCP Ti-Al Alloy Single Crystals. *Metallurgical and Materials Transactions A*, Volume 33, pp. 837-850.
- Xu, N., Song, q., Yefeng Bao, Y. J. & Jun Shen, X. c., 2017. Twinning-induced mechanical properties' modification of CP-Ti by friction stir welding associated with simultaneous backward cooling.
- Yu-ichi, K., Hidenori, T., Keita, S. & Masahiko, I., 2009. Direct Observation of Solidification and Phase Transformation. *Transactions of JWRI, Vol.38 (2009), No. 1*, Jan.
- Zhou, W. & Wang, Z. L., 2006. *Scanning Microscopy for Nanotechnology: Techniques and Applications*. s.l.:Springer.

Appendix A EBSD and TEM study of DMD manufactured cp-TI (grade 2)

Appendix A



Appendix B EBSD and TEM study of DMD manufactured cp-Ti (grade 2)

Appendix B

Here is a small brief of the presentation sent to me by NTiC

Norsk Titanium Components (NTiC) has developed a new technology for efficient production of complex titanium components

Our objective is to produce:

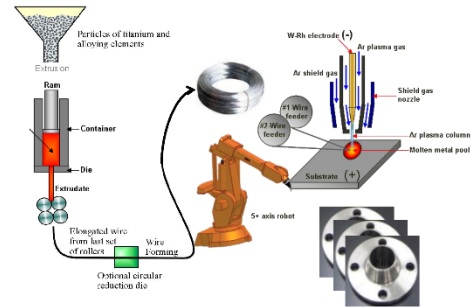
- cost effective and near net shape complex titanium components
- with extensive freedom of design
- and short lead time

This is achieved through a *new and patented technology* using plasma transfer arc (PTA) in a fully automated direct metal deposition (DMD) production process.



NTiC manufacturing technology contains only two main steps, in comparison to conventional method of manufacturing complex Ti components.

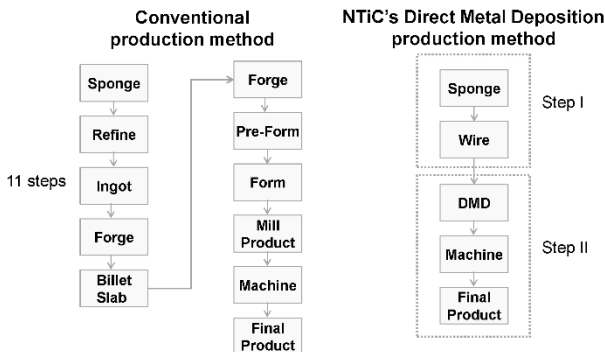
1. Non melt production of titanium wire directly from titanium sponge
2. Direct Metal Deposition (DMD) of near net shape titanium components directly from Ti-wire



Private & Confidential

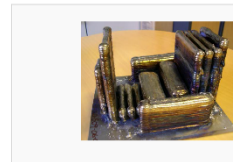
Private & Confidential

NTiC's DMD production method significantly reduces the number of steps from raw material to finished product



Private & Confidential

NTiC's mechanical properties for grade 5 (Ti-6Al4V) are presently between the specifications for forged and casted Titanium



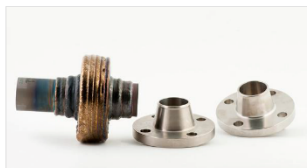
The test results are based on mechanical testing of a block produced as part of qualification for the aerospace industry (October 2011).

Findings: Achieved better than forged material properties in yield strength, ultimate tensile strength, and elongation. Tensile values are between forged and casted values.

	Yield Strength $R_{p0.2}$ (MPa)	Ultimate Tensile Strength R_m (MPa)	Elongation (%)
AIMS 03-18-006 (Forged plate, Aerospace spec.)	830	900	10
IGC 04.40.110 (Casting, Aerospace spec.)	780	860	5
DMD direction	~ 875	~ 930	~ 11
⊥ DMD direction	~ 854	~ 916	~ 14

Private & Confidential

NTiC's mechanical properties for grade 2 exceeds the ASTM specification for forged Titanium



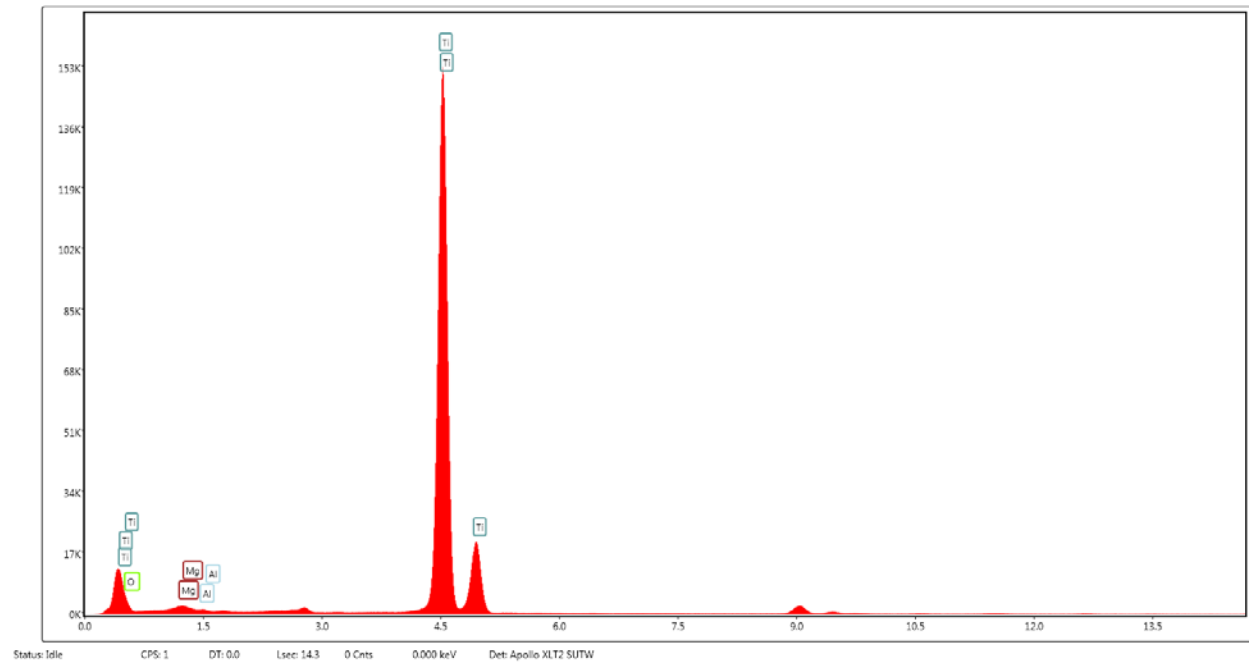
The test results are based on mechanical testing of 12 specimens from flanges produced as part of NORSOK qualification for the Oil & Gas industry (June 2011)

	Yield Strength $R_{p0.2}$ (MPa)	Ultimate Tensile Strength R_m (MPa)	Elongation (%)
ASTM-B381 F-2 Forged ref.	275	345	20
DMD direction	323	419	30.2
⊥ DMD direction	306	404	29.3

Private & Confidential

Appendix C EBSD and TEM study of DMD manufactured cp-Ti (grade 2)

Appendix C



EDS from an area where Mg was detected. It has a very low intensity and was only found in one area, and could not be recreated. It is not included in the result.